Mathematical and Computational Models of the Retina in Health, Development and Disease

Paul A. Roberts[a,b,1,*], Eamonn A. Gaffney[c], Philip J. Luthert[d], Alexander J. E. Foss[e], Helen M. Byrne[c]

[a]*Mathematical Institute, University of Oxford, Andrew Wiles Building, Radcliffe Observatory Quarter, Woodstock Road, Oxford, OX2 6GG, UK*
[b]*Department of Computer Science, University of Oxford, Wolfson Building, Parks Road, Oxford, OX1 3QD, UK*
[c]*Wolfson Centre for Mathematical Biology, Mathematical Institute, University of Oxford, Andrew Wiles Building, Radcliffe Observatory Quarter, Woodstock Road, Oxford, OX2 6GG, UK*
[d]*Institute of Ophthalmology, University College London, 11-43 Bath Street, London, EC1V 9EL, UK*
[e]*Queen's Medical Centre, Department of Ophthalmology, Derby Road, Nottingham, Nottinghamshire, NG7 2UH, UK*

Abstract

The retina confers upon us the gift of vision, enabling us to perceive the world in a manner unparalleled by any other tissue. Experimental and clinical studies have provided great insight into the physiology and biochemistry of the retina; however, there are questions which cannot be answered using these methods alone. Mathematical and computational techniques can provide complementary insight into this inherently complex and nonlinear system. They allow us to characterise and predict the behaviour of the retina, as well as to test hypotheses which are experimentally intractable. In this review, we survey some of the key theoretical models of the retina in the healthy, developmental and diseased states. The main insights derived from each of these modelling studies are highlighted, as are model predictions which have yet to be tested, and data which need to be gathered to inform future modelling work. Possible directions for future research are also discussed.

Whilst the present modelling studies have achieved great success in unravelling the workings of the retina, they have yet to achieve their full potential. For this to happen, greater involvement with the modelling community is required, and stronger collaborations forged between experimentalists, clinicians and theoreticians. It is hoped that, in addition to bringing the fruits of current modelling studies to the attention of the ophthalmological community, this review will encourage many such future collaborations.

Keywords: Oxygen, Neuroglobin, Photoreceptors, Angiogenesis, Retinitis Pigmentosa, Choroidal Neovascularisation.

Contents

1. Introduction

The retina is a complex and highly structured tissue. Covering the inner surface of the back of the eye, it captures incident light, generating electrochemical signals, which, after some initial processing, are transmitted to the brain via the optic nerve, giving rise to visual perception. As such, it is arguably the most important means by which we gain information about the world around us.

The last two decades have seen a rapid increase in the use of mathematical and computational modelling techniques in the biological sciences, due, in part, to an increase in computational

*Corresponding author
Email addresses: p.a.roberts@univ.oxon.org (Paul A. Roberts), gaffney@maths.ox.ac.uk (Eamonn A. Gaffney), p.luthert@ucl.ac.uk (Philip J. Luthert), alexander.foss@nottingham.ac.uk (Alexander J. E. Foss), helen.byrne@maths.ox.ac.uk (Helen M. Byrne)
[1]Present address: School of Mathematics, University of Birmingham, Edgbaston Campus, Birmingham, B15 2TT, UK

[2]ODE: ordinary differential equation, PDE: partial differential equation, Ngb: neuroglobin, RdCVF: rod-derived cone viability factor, MSS: mutant steady-state.

resources. These methods have been applied to a plethora of systems, across a range of spatial and temporal scales, from the ecological, through to the molecular scale and from the evolutionary timescale to the rapid firing of neurons (Keener and Sneyd, 2009a,b; Murray, 2002, 2003). As a consequence, a wealth of insights have been generated that would have been difficult, and in many cases impossible, to achieve through the use of experimental or diagnostic techniques alone.

Table 1: Table of nomenclature. Abbreviations of mathematical and biological terms used within the text are defined.

Mathematical Terms

Term	Definition
ODE	Ordinary Differential Equation
PDE	Partial Differential Equation
1/2/3D	One-/Two-/Three-Dimensional

Biological Terms

Term	Definition
ADP	Adenosine Diphosphate
AMD	Age-related Macular Degeneration
ATP	Adenosine Triphosphate
BM	Bruch's Membrane
CC	Choriocapillaris
CNV	Choroidal Neovascularisation
DA	Dark Adaptation
E •	Embryonic day •
ILM	Inner Limiting Membrane
IPL	Inner Plexiform Layer
IS	(Photoreceptor) Inner Segment
LA	Light Adaptation
MMP	Matrix Metalloproteinases
MSS	Mutant Steady-State
Ngb	Neuroglobin
OPL	Outer Plexiform Layer
OS	(Photoreceptor) Outer Segment
P •	Post-natal day •
PDGF-A	Platelet-Derived Growth Factor A
POS	Photoreceptor Outer Segment
RdCVF	Rod-derived Cone Viability Factor
RP	Retinitis Pigmentosa
RPE	Retinal Pigment Epithelium
RVP	Retinal Vascular Plexus
VEGF(-A)	Vascular Endothelial Growth Factor (A)

The revolution in mathematical and computational biology has not left eye and retinal research untouched, with a host of models exploring the biomechanics of the eye (Burd and Regueiro, 2015; Ethier et al., 2004; Grytz and Meschke, 2010; Grytz et al., 2011; Ruberti et al., 2011), glaucoma (Band et al., 2009; Burgoyne et al., 2005; Harris et al., 2013; Sigal and Ross Ethier, 2009), flow within the aqueous and vitreous humours (Siggers and Ethier, 2012; Stewart et al., 2014) and the dynamics of the tear film (Braun, 2012; Braun et al., 2015; King-Smith et al., 2008). A number of models of the retina have also been developed, though modelling in this area has been less extensive than that devoted to other aspects of the eye. The purpose of this review is to highlight insights that have been gained from theoretical studies of the retina and to stimulate further modelling work and theoretical/experimental collaborations in this area.

Whilst experimental and clinical studies can reveal many of the physiological and biochemical details of the retina, there are limits to the questions that can be answered using these techniques alone. Mathematical and computational modelling allows us to extend these horizons in at least three ways. Firstly, it allows us to understand and predict the behaviour of systems which involve *nonlinearities*, such as those generated by feedback mechanisms in biochemical reaction networks, or those which arise in the mechanics of fluid flow (see Sections 3.3 and 5.1.1 for examples). The sensitivity of the system to alterations in each component can be tested, and the range of qualitative behaviours that it may exhibit, together with the conditions under which they are realised, may be determined. Thus, by placing a problem in a modelling framework, we gain insight into why a system behaves as it does, when it does. Secondly, modelling allows us to *isolate mechanisms*, or manipulate a system, in ways that may not be possible experimentally. An example of this is discussed in Section 5.1.3, where oxygen toxicity is assumed to be the only cause of photoreceptor death in retinitis pigmentosa. Lastly, modelling allows examination of a *wider range of scenarios* than would be possible experimentally, since *in silico* (computer simulation) studies are not subject to the same financial and time constraints as those performed *in vivo* or *in vitro*. This is seen clearly in Section 5.2, where the effects of a range of inter-cell adhesivities on the progression of choroidal neovascularisation are investigated.

How, then, can mathematical and computational models be integrated with experimental and clinical studies? In Figure 1, we sketch out the basic contours of this relationship. We begin with the system to be modelled and all that is known about it. Upon this foundation, and guided by a set of well-defined questions, we build our theoretical model. In so doing, we make a series of *simplifying assumptions*, including only those features of the system which are thought to be significant and of relevance to the questions under consideration. The nature of the system and the questions we bring to it will also influence the type of model we develop (see Section 2 for a discussion of model types). Having formulated our model, we use *mathematical analysis* and/or *computational simulations* to derive solutions. Comparing these solutions with our current knowledge, we find that the model is either successful or unsuccessful in replicating its known behaviours. If unsuccessful, the model is revised and fresh solutions generated; if successful, the model is then used to make *predictions* that lie outside our knowledge domain, in an attempt to answer our earlier questions. These predictions may then be tested experimentally. If the experiments match with model predictions then we may have some confidence that we have answered our questions, whilst if they do not, then we must revise our model and compare it once more with known system behaviour, returning to

an earlier point in the *modelling/experiment cycle*. Insight is gained at two main stages during this process. Firstly, insight is gained at the *benchmarking* stage (see Figure 1), which reveals whether or not the mechanisms included in the model are sufficient to replicate known behaviour. Secondly, insight is gained when experimental/clinical studies confirm model predictions (see Figure 1).

The above description does not perfectly represent the approach taken in all of the modelling studies presented below, but it serves as a basic framework. Depending upon what data are available, it may be difficult to benchmark the model and many modelling predictions are left to gather dust without experimental confirmation. It is important to note that it is unhelpful to simply characterise models as either right or wrong, since any model is a *simplified representation of reality* and hence always, in some sense, wrong. A more fitting way of classifying them would be as *useful* or *useless*. A model is useful if it replicates current data enabling us to make predictions, or if it fails to replicate current data, but in such a way as helps us to identify missing or unwarranted features of the model. It is useless if it fails in both of these respects.

The process of constructing a mathematical model is itself informative, as it forces us to think about the biological system in a new way, formalising and consolidating the questions being addressed. Whilst the primary motivation for modelling arises from questions raised by experimentalists, it is often not until this stage, or those which follow, that many of the questions that we wish to pose to the model occur to us; insights emerging unexpectedly and unlooked for, as a result of this new way of thinking.

The remainder of this paper is structured as follows. In Section 2, we review some of the mathematical and computational techniques used in the modelling studies discussed in this paper. In Sections 3–5, we examine a set of retinal models from across a range of *healthy*, *developmental* and *diseased* states. In each case, we describe the problem, the model and the results generated, comparing them with experimental and clinical data. Testable model predictions are highlighted, as are areas where more experimental data are needed to inform future modelling studies. Lastly, in Section 6, we summarise the state of the field and suggest directions for future research. See Table 1 for definitions of the abbreviations used within the text.

2. Mathematical and Computational Modelling

In seeking to mathematically describe a biological system, we must choose between a range of *model types*. Whilst there may be no unique best model, our selection will be guided by the form of the system and the questions which we aim to address. Each type of model has *advantages* and *disadvantages* and will involve making simplifying assumptions. Table 2 provides an overview of the available options. In what follows, we summarise some key model types. This is not intended as a comprehensive overview; rather, it is tailored to the modelling studies that are presented in the remainder of this paper.

Phenomenological models are designed simply to fit with experimental data, and neglect the underlying mechanisms that gave rise to them, whereas *mechanistic models* are designed to describe the underlying processes, such that, if they are accurate, behaviour consistent with the data will emerge naturally from the system. (In practice, no model is fully mechanistic, its components reducing at some level to the phenomenological.) For example, suppose that we were modelling the production of a chemical by a cell population, where the quantity of the chemical increases linearly over time. A phenomenological model might simply fit a straight line to the data, giving $y = at + b$, where y is the chemical concentration, t is time, and a and b are constants which are chosen to give a good fit to the data. By comparison, a mechanistic model might describe the various sub-cellular mechanisms which give rise to the production of the chemical, such that, if the model is accurate, it replicates the linear dynamics. The models presented below are all mechanistic.

As the title of this paper indicates, we distinguish between *mathematical* and *computational models*, though we note that this is not a sharp distinction, there being areas of overlap between the two model types. Broadly speaking, computational models require simulation to reveal their behaviours, whereas the behaviour of mathematical models can be revealed by the application of analytical techniques (see the discussion of analytical techniques below). Typically, mathematical models comprise only a few equations (the trophic factor model in Section 5.1.1 contains no more than 4 governing equations), whilst computational models involve either a large system of equations and/or an algorithmic component (see, for example, the choroidal neovascularisation model in Section 5.2, where the movement of cells is described algorithmically). Thus, computational models tend to be more comprehensive, whilst mathematical models allow for a more intuitive understanding of the system.

If a system is homogeneous or spatial variation is unimportant, then a *well-mixed*, spatially-independent model may be used (this is the case in the trophic factor model in Section 5.1.1, where the spatial distribution of rods and cones is ignored), the focus being the temporal evolution of the system. If, however, spatial structure is important, then either a *compartmental* or *spatial model* is required. Compartmental models decompose the system into a set of spatially homogeneous compartments, with terms to describe how material may be exchanged between them (for instance, the toxic substance model in Section 5.1.2 identifies each photoreceptor with an individual compartment, governed by its own equation), whilst fully-spatial models allow for spatial heterogeneity within the same compartment (see, for example, the models of retinal oxygen distribution in Section 3.1, where the oxygen concentration is allowed to vary across each model layer).

If we are interested simply in the resting state of a system, then a *steady-state model* (in which the system does not change with respect to time) can be used, whereas, if the dynamic behaviour of the system is important, then a *time-dependent model* is needed (where the system evolves over time). For example, the oxygen distribution models in Section 3.1 are of the steady-state form, oxygen profiles being assumed to change very little under normal conditions, whilst the photoreceptor models

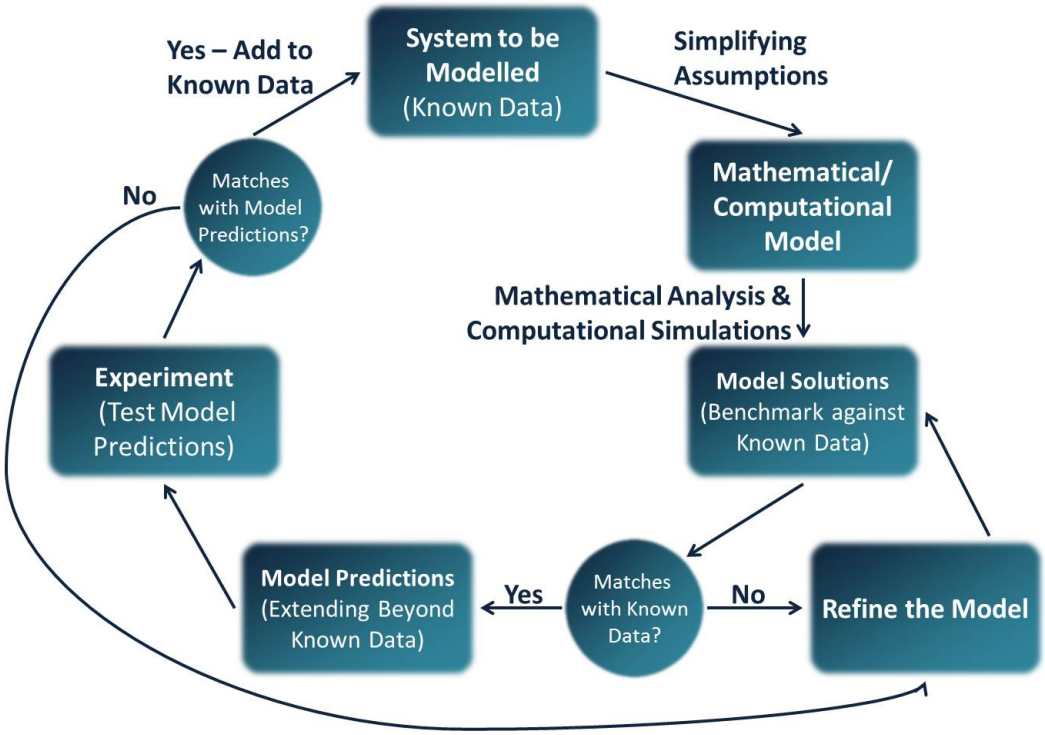

Figure 1: The experiment/modelling cycle. Mathematical and computational models are derived to answer questions arising from what is known about the biological system. Model solutions are then compared with known data and refinements to the model are made where necessary. Once successfully benchmarked, the model is used to make predictions which may then be tested experimentally. Further model refinements may be necessary at this stage. Agreement between modelling predictions and experimental results gives us confidence that we have gained reliable new knowledge about the system.

in Section 3.4 are time-dependent, so that they can capture the time variation in outer segment length.

If the objects being modelled (e.g. cells or molecules) are numerous and small in relation to the spatial domain in which the model is being solved, then cell populations may be treated as continuous densities and chemicals as concentrations (see, for example, the oxygen toxicity models in Section 5.1.3, where photoreceptors are treated as densities and oxygen as concentration). *Continuum models* may be analytically tractable, allowing us to derive analytical solutions (see below) and hence predict how a system will behave under different conditions. If the above assumptions do not hold, then a discrete model is appropriate. *Discrete models* may incorporate more details than continuous models, but are more computationally expensive, with computational costs increasing dramatically as the number of objects is increased. For example, the retinal angiogenesis model in Section 4.1 treats blood vessels as discrete entities, allowing it to capture their intricate spatial structure.

Lastly, a distinction may be made between *deterministic* and *stochastic models*. Deterministic model simulations run under the same conditions always produce the same solution (see, for example, the choriocapillaris blood flow models in Section 3.3), whilst stochastic models incorporate a probabilistic element, capturing the 'noise' of a biological system, as a result of which, each simulation is different (an example being the stochastic apoptosis of photoreceptors in the toxic factor model in Section 5.1.2, see de Vries et al. 2006 for a description of stochastic techniques). In recent years, continuous-deterministic and discrete-stochastic models have been combined in what are known as *hybrid models* (as in the retinal angiogenesis model in Section 4.1).

Continuous-deterministic models are typically described in terms of *ordinary differential equations* (ODEs) and *partial differential equations* (PDEs). ODEs are used in well-mixed and compartmental models, where they describe the evolution of the system with time (e.g. Sections 5.1.1 and 5.1.2), and are also used in one-dimensional (1D) steady-state models (e.g. Section 3.1). PDEs are used for dynamic spatial models in 1D, 2D or 3D and for steady-state models in 2D or 3D (e.g. Section 5.1.3).

In defining a problem, a number of factors must be taken into consideration. Firstly, where the model is spatial, we must describe the (1D/2D/3D) *geometry* of the domain (region in space) on which the problem is to be solved. *Governing equations* must be imposed in the domain, and combined with *initial conditions* (to describe the state of the system at time $t = 0$) and *boundary conditions* (to describe the behaviour of the problem at the domain boundaries). Lastly, values must be assigned to the *model parameters*, using experimentally measured data where possible.

Having defined a model, we may investigate its behaviour. Typically, the models which arise from biological problems do not admit explicit *analytical solutions*. That is, we cannot find algebraic expressions for the dependent variables (e.g. cell density or chemical concentration) in terms of the independent vari-

Table 2: Model types. Contrasting types of models are described and their advantages and disadvantages noted.

Model Type	Description/Assumptions	Advantages	Disadvantages
Phenomenological vs	Designed to match the experimental data	Close fit to data	Little insight
Mechanistic	Designed to capture the underlying processes	Insight generated	Loose fit to data
Mathematical vs	Fully described by a set of mathematical equations Relatively simple	Analytically tractable and generally not computationally expensive	Lacks detail
Computational	Require simulation to reveal their behaviour Typically complex	Detailed	Not analytically tractable and often computationally expensive
Well-mixed vs	Spatial structure and effects are neglected	More tractable	Spatial effects neglected
Compartmental/Spatial	Spatial distributions and compartmentalisation are accounted for	Spatial effects captured	Less tractable
Steady-state vs	The system does not vary in time	More tractable	Dynamics lost
Time-dependent	The system may evolve over time	Dynamics captured	Less tractable
Continuous vs	The system is continuous in space and time	More analytically tractable and generally not computationally expensive	Details lost
Discrete	The system moves between discrete states in space and time	Many details captured	Less analytically tractable and often computationally expensive
Deterministic vs	Simulations run under the same conditions produce the same solution	Substantial analytical insight	Does not account for noise
Stochastic	The model contains a probabilistic component Simulations run under the same conditions produce different solutions	Accounts for noise	Little analytical insight

ables (space and time) together with the model parameters. Instead, we must proceed in one or both of the following two ways. Firstly, we may solve our equations *numerically*. For ODE and PDE models, this may involve methods such as the finite difference method (or method of lines) and the finite element method, which involve discretizing our equations in space and time (see Morton and Mayers, 2005; Süli and Mayers, 2003, for details). Secondly, we may use *analytical methods* to systematically reduce the governing equations to a simpler form. Commonly used analytical methods include asymptotic analysis, which reduces the system to its dominant components, and steady-state and bifurcation analyses, which allow us to determine the stability properties of the system i.e. whether the system behaviour is insensitive to small perturbations, and how such responses vary as parameters are altered (see Howison, 2005; Strogatz, 1994, for details). Often, a combination of numerical and analytical techniques is used to provide a more complete picture, consistent results giving an added degree of confidence in the model and solution methods. Lastly, since the parameter values in our models are frequently estimated and often subject to variability, *sensitivity analyses* may be performed to determine the effect of parameter variation on model predictions.

3. Health

3.1. Retinal Oxygen Distribution

The mammalian retina has a multilayered structure consisting of numerous cell types (see Figure 2). The *outer retina* contains two cellular layers: the *retinal pigment epithelium* (RPE) and the light-detecting *photoreceptors*, which can be characterised as either *rods* or *cones*, whilst the *inner retina* also contains two cellular layers: a layer consisting of bipolar, horizontal, amacrine and Müller cells, and the ganglion cell layer. The inner layers are responsible for preprocessing of visual information and its subsequent transmission to the brain, via the optic

nerve and are separated from the vitreous humour by the *inner limiting membrane* (ILM).

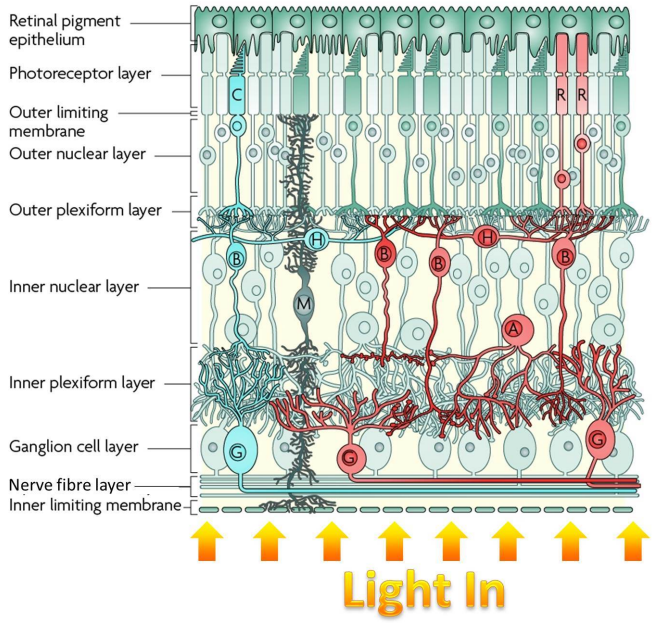

Figure 2: Diagram of the human retina. The retina is composed of four cellular layers: the outer retina contains the retinal pigment epithelium and photoreceptor layers, whilst the inner retina contains bipolar/horizontal/amacrine/Müller glial cell and ganglion cell layers. The diagram is oriented such that the top lies outermost and the bottom innermost in the eye. R: rod photoreceptor. C: cone photoreceptor. H: horizontal cell. B: bipolar cell. M: Müller glial cell. A: amacrine cell. G: ganglion cell. Figure reproduced, with permission and modifications, from Swaroop et al. (2010), where modifications are reproduced, with permission, from Roberts et al. (2015).

The retina consumes oxygen at a higher rate than most other tissues in the mammalian body (Anderson, 1968; Anderson and Saltzman, 1964; Wangsa-Wirawan and Linsenmeier, 2003; Yu and Cringle, 2001). To meet this need, it is equipped with an extensive vasculature. The outer retina is supplied mainly by the *choroid*, which lies outward from the retina, separated from the RPE by Bruch's Membrane, whilst the inner retina is supplied by *retinal capillary layers*, of which there are typically two, one deep and the other superficial (though this number varies between regions, see Chan et al., 2012; Kur et al., 2012; Michaelson, 1954; Pournaras et al., 2008; Snodderly et al., 1992; Tan et al., 2012, for more details). The magnitude of oxygen supply and demand render the retina vulnerable to both *hypoxia* (oxygen deprivation) and *hyperoxia* (toxically high oxygen levels). Therefore, it is of interest to understand how the retina is maintained in *normoxia* (favourable oxygen levels) in health, and how and why the oxygen profile changes in disease states such as vascular occlusive diseases, diabetic retinopathy, retinopathy of prematurity and retinitis pigmentosa (Wangsa-Wirawan and Linsenmeier, 2003).

Oxygen sensitive microelectrodes have been used to measure the partial pressure of oxygen across the width of the retina, from the ILM to the choroid, in a variety of mammals and under a range of conditions (see Wangsa-Wirawan and Linsenmeier, 2003; Yu and Cringle, 2001, 2005; Yu et al., 2013, for reviews). Whilst it is helpful to determine the oxygen profile (comparisons between profiles providing insight even in the absence of a model), the measurement does not, by itself, help us to understand why the profile takes the shape that it does. In order to explain the profile, we must determine the rates of oxygen supply and demand, and how these vary across the retina.

A number of mathematical models have been developed to describe and explain retinal oxygen measurements. These models typically assume that the system is at *steady-state* (i.e. not varying with time) and are posed on a *one-dimensional Cartesian geometry*, across the width of the retina, perpendicular to the wall of the eye. Using a Cartesian geometry, rather than a spherical geometry, is justified, since the width of the retina is much smaller than the radius of curvature of the eye. It is further typically assumed that the rate of oxygen consumption is *piecewise constant* across the retina. As such, the retina is decomposed into a series of n *discrete intervals* $0 < x < L_1$, $L_1 < x < L_2, \ldots, L_{n-1} < x < L_n$ (see Figure 3), where x is the distance from the *choriocapillaris* (CC, the innermost layer of the choroid). Within each interval, the rate of oxygen uptake is given by a constant, Q_i (for $i = 1,\ldots,n$). Therefore, invoking Fick's second law, these models reduce to the following ODEs:

$$D\frac{\mathrm{d}^2 c}{\mathrm{d}x^2} = Q_i, \qquad \text{for } i = 1,\ldots,n, \tag{1}$$

where $c(x)$ is the oxygen concentration and D is the diffusivity of oxygen. These equations may be solved to give

$$c(x) = \frac{Q_i x^2}{2D} + A_i x + B_i, \qquad \text{for } i = 1,\ldots,n, \tag{2}$$

where the constants of integration, A_i and B_i ($i = 1,\ldots,n$), are determined by imposing boundary conditions at all external and internal boundaries. As such, the profiles are *piecewise linear* (for $Q_i = 0$) and *quadratic* (for $Q_i \neq 0$), where $Q_i > 0$ indicates a net *uptake* and $Q_i < 0$ a net *supply* of oxygen.

To date, most models have restricted their attention to the avascular outer retina (Dollery et al., 1969; Haugh et al., 1990; Linsenmeier, 1986). Since the inner retinas of most mammals are penetrated by deep and superficial retinal capillary beds, it is not possible, using these models, to distinguish between oxygen supply and consumption in this region. Two resolutions to this problem have typically been considered: using animals with avascular inner retinas such as the rabbit or guinea pig (Cringle et al., 1996; Stefánsson, 1988), or occluding the retinal capillaries (Braun et al., 1995; Dollery et al., 1969). In this way, the models can be extended to describe the entire retina, and the oxygen consumption of each layer determined. Other authors include the inner retina without occlusion, but cannot distinguish between supply and uptake in those layers in which capillaries are present (Cringle and Yu, 2002).

In many theoretical studies, the number of model layers is varied to determine the minimum number required to obtain a good fit to experimental data, the number being increased until the improvement in fit is deemed insignificant, or the model becomes sensitive to noise in the data

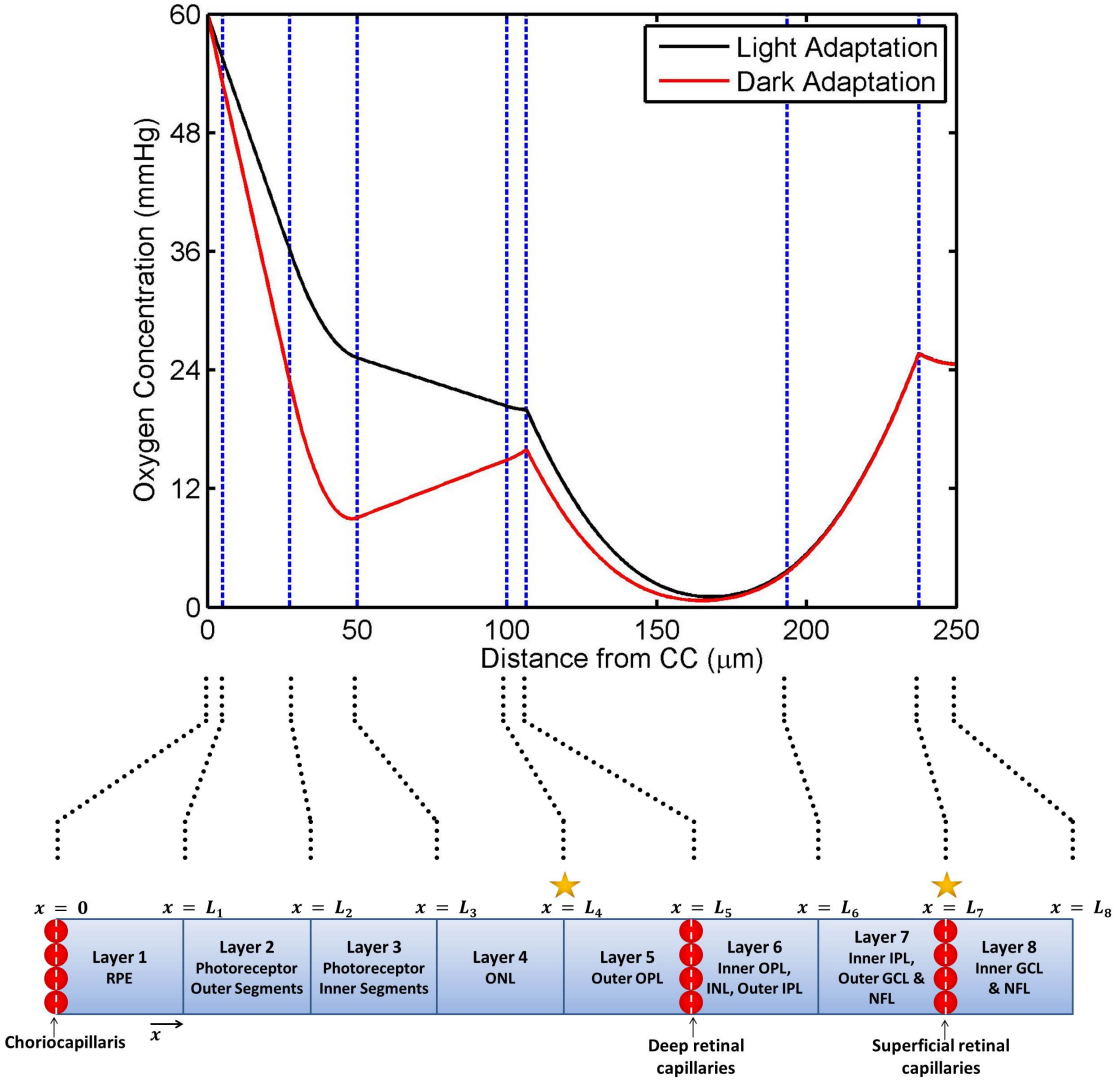

Figure 3: Roberts et al.'s retinal oxygen distribution model. Bottom: diagram to show the model geometry. Oxygen is supplied to the tissue via the CC and retinal capillaries, whilst the net-flux of oxygen at $x = L_8$ is zero. The concentration and flux of oxygen is continuous across all other boundaries. The flux of neuroglobin (Ngb) between layers is zero, except at those boundaries marked with stars, across which the concentration and flux of Ngb is continuous. In the case where Ngb is not included, layers 6 and 7 may be combined, reducing the model to 7 layers. Top: simulation results showing the oxygen distribution in the healthy human retina under LA and DA in the absence of Ngb. The spatial extent of the model layers is depicted by the dashed vertical lines. The oxygen concentration in the outer retina (layers 1–5) and layer 6 is significantly lower under DA, due to the increased rate of oxygen uptake by the photoreceptor ISs. CC: choriocapillaris, RPE: retinal pigment epithelium, ONL: outer nuclear layer, OPL: outer plexiform layer, INL: inner nuclear layer, IPL: inner plexiform layer, GCL: ganglion cell layer, NFL: nerve fibre layer. Figure reproduced, with permission and modifications, from Roberts et al. (2015).

(Braun et al., 1995; Haugh et al., 1990; Linsenmeier, 1986). The earliest such models are those of Dollery et al. (1969) who used single layer models for the outer retina and the whole retina. Later, Linsenmeier (1986) and Stefánsson (1988) developed two layer models for the outer retina and for the inner and outer retina respectively. This was followed by a three layer model of the outer retina (Haugh et al., 1990), to which a fourth layer was later added, to encompass the inner retina (Braun et al., 1995). The most detailed model of this type to date is that due to Cringle and Yu (2002), who decompose the retina into eight layers. Model layers representing either entire *cellular layers* (e.g. the ganglion cell layer), or *subcompartments* within cellular layers (e.g. the photoreceptor inner segment layer).

Once the number of model layers has been fixed, the models may be fitted to the experimental profiles by varying the L_is (except L_n, the total retinal width), Q_is and oxygen concentrations on the external boundaries upon which Dirichlet boundary conditions (at which the oxygen concentration is held at a fixed value) have been imposed. In this way, one can determine the (net) oxygen consumption in each layer of the retina and thereby explain why the profile takes the shape that it does.

This approach has led to some important discoveries. For

example, it has been shown that the photoreceptor *inner segments* (ISs) are the dominant oxygen consumers in the outer retina, consuming approximately twice as much oxygen under *dark adaptation* (DA) as under *light adaptation* (LA) (Haugh et al., 1990; Linsenmeier, 1986). Meanwhile, the outer region of the *inner plexiform layer* (IPL) dominates consumption in the inner retina, exceeding that of the photoreceptor ISs (Cringle and Yu, 2002). Other discoveries include an explanation for how inner retinal normoxia is maintained when the oxygen content of inspired air increases, via increased uptake by the *outer plexiform layer* (OPL) and the outer region of the IPL, and how outer retinal *anoxia* (complete oxygen depletion) is prevented under DA in the rat, through increased oxygen delivery from the CC and deep retinal capillary layer (Cringle and Yu, 2002; Yu and Cringle, 2002). (See Wangsa-Wirawan and Linsenmeier, 2003; Yu and Cringle, 2001, 2005; Yu et al., 2013, for detailed reviews.)

Whilst the above models have proved fruitful, they have two key limitations. Firstly, they do not distinguish between uptake and supply in the vascular inner retina, and, secondly, they do not account for the variation in oxygen uptake with local oxygen concentration, this effect becoming significant in those regions where the oxygen profile approaches hypoxic levels.

Roberts et al. (2015) have developed a model which addresses these limitations (see Figure 3, where layers 6 and 7 are combined in this case, reducing the model to 7 layers). Uptake and supply are distinguished by accounting for the retinal capillary layers through boundary conditions between model layers, whilst the dependence of oxygen uptake upon the local oxygen concentration is accounted for by replacing the constant uptake term, Q_i, with a *Michaelis-Menten* term, $Q_i c/(\gamma + c)$, so that equation (1) becomes

$$D\frac{\mathrm{d}^2 c}{\mathrm{d}x^2} = \frac{Q_i c}{\gamma + c}, \qquad \text{for } i = 1,\ldots,7, \tag{3}$$

where γ, the Michaelis constant, is the oxygen concentration at which the oxygen consumption rate is half maximal ($Q_i/2$). The model describes the mid-peripheral human retina (with seven layers required to account for the spatial variation in oxygen consumption and the presence of capillary layers), though it could be adapted to model any mammalian retina by adjusting the number and arrangement of layers and the boundary conditions between layers. As with the previous studies, this model could also be fitted to experimental profiles. Unlike equation (1), equation (3) does not have an analytical (algebraic) solution and so must be solved numerically.

Mathematical analysis of Roberts et al.'s model reveals that the earlier piecewise linear and quadratic models (equations (1) and (2)) are valid, provided the oxygen concentration does not approach hypoxic levels, oxygen levels below 1 mmHg being considered hypoxic (McGuire and Secomb, 2001; Roberts et al., 2015). Quadratic approximations are also valid in hypoxic, or near-hypoxic regions; however, the coefficients must be modified as described in Roberts et al. (2015). This analysis therefore places the previous models on a stronger *theoretical foundation*, whilst also enabling them to be extended to account for a broader range of scenarios.

Whilst Roberts et al.'s model resolves some of the weaknesses in previous models, it has limitations. In particular, by placing capillary layers along the boundaries between model layers, it assumes that the capillaries lie in a plane. Whilst this is reasonable for the two retinal capillary layers in the mid-periphery of the human retina and in the retinas of many other mammals, some capillary layers, such as the additional layers found in the peripapillary area of the human retina, are more diffuse (Chan et al., 2012; Kur et al., 2012; Michaelson, 1954; Pournaras et al., 2008; Snodderly et al., 1992; Tan et al., 2012). In these cases, it would be more appropriate to incorporate a distributed oxygen source term into those layers that contain capillary beds. Provided the capillary surface area, permeability and oxygen concentration could be measured, it would still be possible to distinguish between uptake and supply.

In addition to considering oxygen levels within the retina, modellers have investigated oxygen transport within the *retinal vasculature*. In particular, Liu et al. (2009) constructed a model of the flow distribution and oxygen transport within a 2D retinal arterial network. The central retinal arterial geometry was reconstructed from an image of the human fundus and the peripheral circulation added using a structured tree model, allowing a prediction for the oxygen distribution within a retinal network. Further, Ganesan et al. (2010a,b) created a network model of the murine retinal vasculature, incorporating all three layers (the superficial layer, containing veins and arterioles, and the intermediate and deep capillary networks). The veins and arterioles of the superficial layer were modelled directly using data from the image analysis of the murine retina, whilst the capillary layers were represented using uniformly distributed meshes. This model produced a number of interesting further results; for instance, it was found that the blood *haematocrit* (the ratio of red blood cell volume to total blood volume) is smaller close to the optic disc and greater toward the periphery.

Aletti et al. (2015); Arciero et al. (2013); Guidoboni et al. (2014) and others have constructed both compartmental and 3D models to describe the *autoregulation* of blood flow within the retinal circulation (see, Harris et al., 2013, for a review). These models help to explain and predict the effects of elevated intraocular pressure (an important risk factor for glaucoma) upon retinal hemodynamics, and upon the distribution of oxygen and carbon dioxide within the retinal vascular network. (See also David and Moore, 2008, for a review of models of perfusion and autoregulation in the cerebral vasculature.)

The above models either consider the oxygen distribution across the retina, including the vasculature merely as a source term or boundary condition, or describe conditions within the retinal vasculature, ignoring the oxygen distribution in the surrounding tissue. An early paper by Friedland (1978) considered a simple model of *transmural transport* of oxygen to the retina, in which a single cylindrical capillary exchanges oxygen with a surrounding cylindrical block of retinal tissue (see also, Seth, 2012). More recently, Causin et al. (2015) have produced a more comprehensive model, which couples a description of the blood flow mechanics within the vasculature to a model of the oxygen distribution within the surrounding retinal tissue. The vascular model consists of two components: the arterioles and

venules are represented by networks of discrete fractal trees, whilst the capillary plexuses are represented using a simplified 'lumped' description, consisting of sets of parallel pipes which connect the terminal arterioles and venules (the choroid is not modelled explicitly). This is coupled to a six layer model of the retinal tissue, spanning the width of the retina, between the choroid and the ILM, where the number of layers is chosen to account for variations in oxygen demand between layers and the locations of the capillary plexuses. The model can be used to predict the effects of changes in blood pressure, blood rheology, arterial permeability to oxygen and tissue oxygen demand upon the oxygen distribution within blood vessels and retinal tissue. As yet, no models have been developed to couple the blood flow mechanics within the choroid with the oxygen distribution in the retinal tissue; however, Zouache et al.'s (2015) model, described in Section 3.3, represents a promising step in this direction.

The oxygen distribution within a 2D or 3D block of tissue containing a realistic vascular network can be solved computationally, using either the finite difference or finite element methods. However, this is computationally expensive, since very fine meshes (discretizations of the domain into smaller regions, at the corners of which solutions are calculated) must be used to capture the steep spatial gradients in oxygen concentration. Hsu and Secomb (1989) have developed a '*Green's function method*' to overcome this problem, allowing the oxygen profile within a tissue to be described as the superposition of the oxygen fields produced by discrete sources distributed across the vascular network. This method also overcomes a limitation of the earlier Krogh cylinder model (Krogh, 1919), removing the need to make *a priori* assumptions about the spatial extent of the region of tissue supplied by each vessel segment. In its original formulation, the Green's function method assumed that oxygen consumption was uniform throughout the tissue, required the imposition of (often unrealistic) boundary conditions at the edge of the domain and assumed that the system was at steady-state. These limitations have been successively overcome in a series of subsequent publications (see Secomb, 2015; Secomb et al., 1993, 2004). The Green's function method has also been used by Safaeian and David (2013) to model the oxygen supply to the brain and has great potential for use in similar models of the retina.

In addition to the above retinal oxygen models, Filas et al. (2013) have developed a model for oxygen transport and consumption within the vitreous, accounting for the retina via a boundary condition. It would be interesting to couple this model to models for the oxygen distribution within the retina, such as those developed by Causin et al. (2015); Cringle and Yu (2002) and Roberts et al. (2015) discussed above.

Finally, we note that in order for models to accurately predict retinal oxygen distribution, it is important that the geometry of the retinal vasculature be well-defined. A number of imaging techniques and analyses have been utilised to capture its architecture, including scanning laser ophthalmoscopy (Pellegrini et al., 2014), confocal scanning laser microscopy (Chan et al., 2012; Tan et al., 2012; Yu et al., 2010), optical coherence tomography (Hassenstein and Meyer, 2009; van Velthoven et al., 2007), segmentation algorithms (Giachetti et al., 2014; Pellegrini et al., 2014) and junction resolution algorithms (Al-Diri et al., 2010). See Hassenstein and Meyer (2009); Keane and Sadda (2014); Leontidis et al. (2014); van Velthoven et al. (2007) and Yannuzzi et al. (2004) for reviews.

3.2. Neuroglobin

Given the retina's extensive oxygen demand, any factor which contributes to the supply of oxygen could be vital in preventing hypoxia. It has been suggested that the protein *neuroglobin* (Ngb), which is present in high concentrations in the retina, could enhance the retinal oxygen supply (Burmester et al., 2000). A number of lines of evidence indicate such a role, most notably its similarity in structure and molecular mass to myoglobin; however, opinion about its role remains divided (see Brunori and Vallone, 2007; Burmester and Hankeln, 2004, 2009; Fago et al., 2004; Pesce et al., 2002, for reviews).

In theory, Ngb could enhance the oxygenation of retinal tissue via two distinct yet related processes, namely *transport* and *storage*: Ngb could transport oxygen from regions where it is plentiful to others where it is scarce and provide a temporary supply of oxygen during periods of decreased supply or increased uptake. The first scenario (transport) is best considered using a steady-state (ODE) model, it being assumed that retinal oxygen levels typically remain at steady-state, whilst the second (storage) requires a *time-dependent* (PDE) model.

To date, only two modelling studies have been conducted to investigate the oxygen transport and storage properties of Ngb. Fago et al. (2004) developed a three layer model of the outer retina, consisting of a central region that consumes oxygen and contains Ngb, and two outer layers that do not consume oxygen and are devoid of Ngb. The proportion of Ngb molecules in their oxygen-bound and unbound states is assumed to be at *quasi-steady-state* at all times (that is, the two species are in equilibrium). Their results suggest that the concentration of Ngb in the middle layer would need to exceed 100 μM for Ngb to be effective in storage and to exceed 300 μM to be effective in transport. Since they assume that the local Ngb concentration could not exceed these values, they conclude that Ngb does not play a significant role in transport and storage.

Given that the average Ngb concentration across the retina has been estimated to lie in the range 100–200 μM, Roberts et al. (2015) have argued that, since Ngb is confined to the cytosol of retinal cells and since it is more highly concentrated in some retinal layers than others, the local cytosolic concentrations in some layers could significantly exceed 200μM. They constructed an eight layer model, spanning the full width of the (human) retina and relaxing Fago et al.'s quasi-steady-state assumption (see Figure 3). The model confirmed that Ngb is unlikely to play a significant role in oxygen storage, demonstrating that whilst it will delay a drop in oxygen levels, it will also delay recovery (Roberts, 2015). However, the model suggests that Ngb could prevent hypoxia in the ISs and IPL via transport, increasing oxygen uptake by up to 30–40% in these regions. Further, it was demonstrated, using a simplified, single layer model, that the lower *affinity* for oxygen of Ngb than myoglobin may be advantageous for oxygen transport, contrary to

the prevailing view (Burmester and Hankeln, 2004, 2009; Fago et al., 2004). Indeed, many of the measured Ngb oxygen affinities appear to be close to optimal.

3.3. Choriocapillaris

Zouache et al. (2015) have developed a model to describe the blood flow within the *choriocapillaris* (CC). The CC is the inner layer of the choroid, responsible for supplying the outer retina with oxygen and other nutrients, and for removing waste products. It is subdivided into independent tessellating polygonal units known as *lobules*. These compartments are essentially planar, and are supplied and drained by microvessels, lying deeper in the choroid, via *inlets* and *outlets*, which feed into the outer surface of the lobules, perpendicular to their plane (Zouache et al., 2015). Blood is supplied at the centre of each lobule by an arteriole, and drained at the surrounding vertices by venules. Whilst these compartments are not physically divided from each other, neighbouring outlets are connected by *separatrices* (streamlines which divide the flow into regions with different kinds of motion) in the blood flow, on which the residence time is long, forming an effective barrier between adjacent lobules (Zouache et al., 2015). Lobules are interspersed by avascular *septal pillars*, which stretch between the inner and outer boundaries, interrupting blood flow. The pillars are randomly distributed, with a uniform distribution (Zouache et al., 2015).

Rather than model the entire CC, Zouache et al. (2015) consider an individual lobule. The model is further simplified by decomposing lobules into *triangular prisms*, with the inlet at one vertex and outlets at the other two (see Figure 4(a)). For simplicity, the triangle is assumed to be isosceles, the inlet being separated from the outlets by sides of equal length. The *internal angle at the inlet* and the *septae volume fraction* (the proportion of the domain occupied by septae) are varied to represent lobules at different geographical locations within the eye.

Since the height of a lobule is much smaller than the width of the septal pillars, the component of the flow perpendicular to the inner and outer boundaries can be neglected. Averaging the fluid velocity across the height of the lobule, the model is reduced to a *planar* (2D) flow. The flow is further assumed to be *passive*, driven by the pressure gradient between the inlet and outlets. Blood cells are not modelled explicitly, rather they are assumed to be passive tracers.

The model is used to determine how the *pressure drop* (between the inlet and outlets) and average fluid particle *residence time* (average time spent by blood corpuscles in the lobule) depend upon the internal angle at the inlet and the septae volume fraction.

In the absence of septae, a separation (stagnation) streamline divides the triangle in two, running from the inlet, to a stagnation point on the opposite side of the triangle, midway between the two outlets (see Figures 4(b) and (c)). The pressure drop is minimised, and the average residence time maximised, when the inlet angle is 90°, whilst the pressure drop increases and the residence time decreases as the inlet angle approaches 0 or 180°. The residence time is lower along streamlines close to the walls of the domain, and increases along streamlines approaching the stagnation streamline. As the septae volume fraction increases, the pressure drop and bulk flow velocity increase and the average residence time decreases (see Figures 4(d) and (e)). However, the septae also increase the residence time in the stagnation regions created on their surfaces where the streamlines separate.

As lobule geometry varies across the eye, so too does the pressure drop, blood velocity and residence time. It may be that this variation in geometry is the means by which the exchange of oxygen and other nutrients is modulated to match supply with demand. This *spatial variation* could also help to explain the geographical heterogeneity in vulnerability seen in retinal diseases such as *retinitis pigmentosa* (RP) and *age-related macular degeneration* (AMD) (Zouache et al., 2015). It has been noted that drusen tend to form near venular openings in AMD (Friedman et al., 1963). This model suggests a possible explanation, since it predicts that the residence time of fluid particles is greatest here (Zouache et al., 2015).

Whilst this model provides a useful first step in mathematically describing the CC, it has several limitations. In particular, it does not capture the movement of fluid between the CC and the retina, nor does it account for the three-dimensional nature of the flow, which could have a significant effect on residence time. Zouache et al. are now developing a 3D Navier-Stokes, advection-diffusion model to address these limitations (Zouache et al., 2015). A further interesting extension would be to couple models of the CC to models of the retina in disease states such as RP and AMD, where the supply of oxygen and other nutrients may be critical in driving the disease progression.

Zouache et al.'s work has also served to highlight shortcomings in existing experimental data. In particular, the interior angle at the inlet has not been investigated and, as yet, only one measurement for the pressure drop between inlet and outlet has been published. Zouache et al.'s models show that both of these features are of critical importance for blood flow within the CC and, as such, their accurate measurement should present a promising direction for future experimental research.

3.4. Photoreceptors

A number of models considering either individual photoreceptors or groups of photoreceptors in health have been developed. These models focus on processes such as retinal light adaptation, phototransduction (see in particular Lamb and Pugh Jr., 2004; Sneyd and Tranchina, 1989; Tranchina et al., 1991), photoreceptor and horizontal cell interactions, circadian rhythms (Camacho et al., 2004), information processing (Song et al., 2009, 2012) and receptive fields. Many of these studies are reviewed in Keener and Sneyd (2009b), Chapter 22, to which the reader is referred for further details.

Here we discuss more recent work by Macdougall (2015), which provides a potential explanation for the observed *diurnal variation* in *rod* photoreceptor *outer segment* (OS) length. Each rod OS is composed of a stack of approximately 700–1200 membranous *discs* (Young, 1971). Discs are continuously replenished from the base of the OS, where it meets the IS,

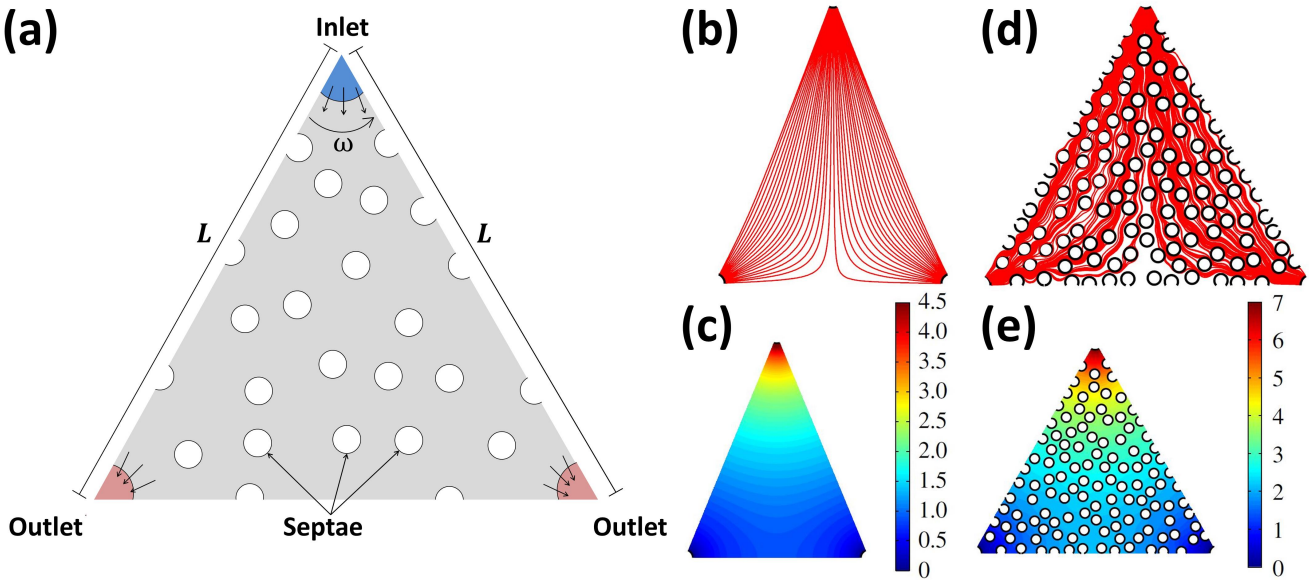

Figure 4: Zouache et al.'s model of blood flow in the choriocapillaris. (a) diagram to show the model geometry, including septae (represented by circles). Lobules are decomposed into isosceles triangular prisms, the inlet (top corner) being separated from the outlets (bottom corners) by sides of equal length (L). The internal angle at the inlet is denoted by ω. Figure adapted from Zouache et al. (2015). (b) and (c) flow streamlines (showing the paths followed by fluid particles, (b)) and pressure field (c) in the absence of septae ($\omega = 45°$). (d) and (e) flow streamlines (d) and pressure field (e) in the presence of septae ($\omega = 60°$). Figures (b)–(e) reproduced, with permission, from Zouache et al. (2015).

whilst groups of discs at the outer tip of the OS are intermittently shed and subsequently phagocytosed by the underlying RPE, the most significant shedding event occurring at the onset of LA (Young, 1967, 1971, 1978; Young and Bok, 1969). As a consequence, the OS is completely replaced over a period of 9–13 days (as measured in the rhesus monkey and assumed to hold true in humans, Young, 1971). Rod OS length varies over a daily cycle, growing under DA and shrinking under LA, indicating that the shedding and renewal rates vary with illumination (Abrámoff et al., 2013).

Macdougall (2015) construct three spatially-resolved continuum models, each testing a different hypothesis, proposed to explain the observed differences in OS length under DA and LA. The first model tests the hypothesis that the observed dynamics can be explained by changes in the *oxygen landscape* between DA and LA, whilst the second tests the hypothesis that the dynamics can be explained by changes in the *phosphocreatine shuttle-derived ATP* concentration in the OS between DA and LA. Both models fail in important respects (see below). Therefore, the third model proposes that a *combination* of changes in the oxygen and phosphocreatine shuttle-derived ATP concentrations is sufficient to explain the OS dynamics. All three models consist of PDEs and ODEs, where the PDEs are defined on a 1D domain spanning the region between the inner end of the IS and the outer end of the OS, the former boundary being fixed in space and the latter free to move (see Figure 5(a)). In each case, it is assumed that the choroid is the sole supplier of oxygen.

The first model consists of a PDE for oxygen concentration and an ODE for OS length. Oxygen diffuses freely across the photoreceptor and is taken up at a baseline level across the domain, with an additional consumption term in the IS to model mitochondrial uptake there, which increases under DA (see Section 3.1). The OS length increases or decreases at a rate proportional to the difference between a predefined *threshold concentration* and the oxygen concentration at the inner end of the IS. The length increases when the oxygen concentration at the inner tip of the IS is above the threshold (i.e. in abundance), and decreases when the oxygen concentration is below the threshold (i.e. in short supply).

The model admits unique, positive, steady-state solutions for OS length under both DA and LA. Simulations capture a *24 hour cycle*, starting with the light adapted steady-state solution at $t = 0$ hours, followed immediately by DA, switching to LA at $t = 12$ hours. The only parameter which changes between DA and LA is the rate of oxygen uptake in the IS. It is found that OS length increases under LA and decreases under DA, behaviour which is the *reverse* of that seen *in vivo*. This result is robust under parameter sensitivity analysis and suggests that oxygen cannot be the sole regulator of OS length.

The second model focusses on how the spatial distributions of creatine phosphate, creatine, free phosphate, ATP and ADP change over time and regulate OS length (see Figure 5(a)). ADP combines reversibly with phosphate to form ATP. The dominant source of ATP is assumed to be that formed by oxidative phosphorylation in the IS mitochondria, rather than that formed by glycolysis throughout the photoreceptor. Consequently, ATP production is neglected in the OS. Dephosphorylation is assumed to be negligible in the OS under DA. However, the demand for ATP in the OS increases under LA, such that dephos-

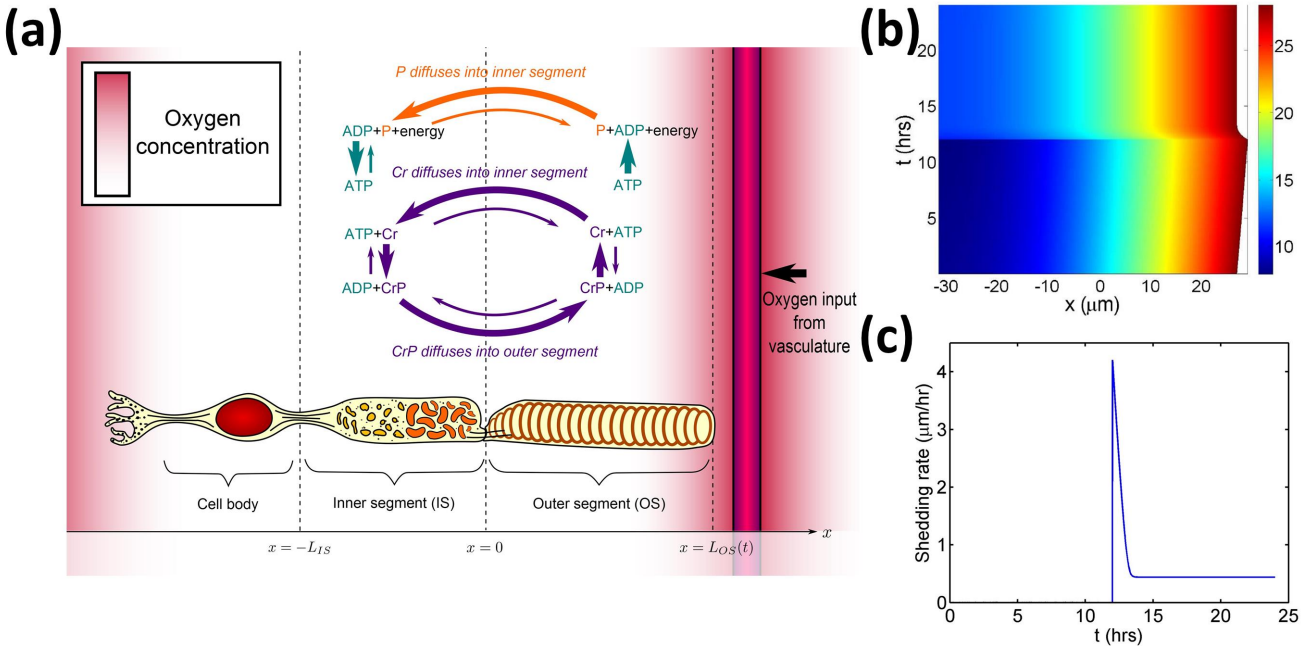

Figure 5: Macdougall's model of photoreceptor shedding and regrowth. (a) diagram showing the model geometry, the oxygen distribution, and the kinetics and dynamics of the phosphocreatine shuttle. The photoreceptor IS has a fixed length, spanning the region between $x = -L_{IS} < 0$ and $x = 0$, whilst the OS length varies with time, t, spanning the region between $x = 0$ and $x = L_{OS}(t) > 0$. Oxygen, phosphocreatine (CrP), creatine (Cr) and phosphate (P) diffuse freely across the domain, whilst none of the species can leave the photoreceptor. Diffusive transport of ATP and ADP is neglected. ADP and P combine reversibly to form ATP, whilst CrP and ADP react reversibly to form Cr and ATP. Larger arrows show the dominant direction of each reaction. (b) simulation results for the third (combined) model, showing the growth and shrinkage of the OS over a 24 hour dark/light cycle, where the heat map represents the oxygen profile (in units of μM) internal to the photoreceptor. The simulation is initiated at the LA steady-state, grows under dark conditions for the first 12 hours and shrinks under light conditions from 12 to 24 hours. (c) graph to show the evolution of the shedding rate over time for the simulation depicted in (b). Shedding is absent under DA, but occurs under LA, reaching its highest rate shortly after the onset of LA. Figures (a) and (b) reproduced, with permission and modifications, from Macdougall (2015), where the diagram of the photoreceptor in (a) is adapted from Young (1967). Figure (c) supplied by Macdougall and reproduced with permission.

phorylation occurs under LA. The diffusion rates of ATP and ADP are slow and, hence, neglected. Therefore, in order for IS-produced ATP to reach the OS, it must do so via the *phosphocreatine shuttle*: creatine binds ATP reversibly to form creatine phosphate and ADP, the forward reaction being favoured in the IS and the reverse in the OS. Creatine phosphate, creatine and phosphate are all free to diffuse across the photoreceptor, resulting in a net flux of creatine phosphate from the IS to the OS, and of creatine and phosphate from the OS to the IS. Since the ATP and ADP concentrations evolve on a much faster timescale than those of the other reactants, they are assumed to be at quasi-steady-state, so the system comprises 3 PDEs for phosphocreatine, creatine and phosphate. The OS is assumed to grow at a constant rate and to shed discs only when the ATP concentration at the outer tip of the OS falls beneath a threshold value, corresponding to a *critical OS length*, at which point shedding proceeds at a rate proportional to the amount by which OS length exceeds this critical length.

Simulations for the 24 hour dark/light cycle predict that the OS will shed discs under LA, causing it to shrink towards a steady-state (after about 2 hours), in agreement with *in vivo* observations. The OS length increases linearly under DA; however, it does not reach steady-state, growing *unboundedly* if DA is maintained indefinitely. These results suggest that the phosphocreatine shuttle is sufficient to regulate OS length under LA, but not under DA.

The third model combines the hypotheses of the two previous models. Simulations of the combined model show OS growth under DA and shrinkage under LA, in agreement with *in vivo* observations (see Figure 5(b)). The decrease in IS oxygen consumption leads to growth under LA; however, rapid shedding dominates growth at the onset of LA (as observed in Young, 1978) leading to net OS shrinkage (see Figure 5(c)). The shedding rate subsequently decreases, balancing growth, such that the system approaches, and effectively reaches, steady-state under LA. Growth under DA is both linear and *bounded*, improving on both of the previous models; however, OS growth does not reach steady-state until approximately 100 hours. Whilst one would expect growth to stall earlier than this *in vivo*, these results are supported by a study carried out by Bassi and Powers (1990) on goldfish, which showed that OS length increases at a constant rate when dark conditions are sustained for 7 days. In an ordinary light/dark cycle, the onset of LA interrupts growth under DA, such that continued growth beyond the physiological norm is not realised.

Many retinal diseases (e.g. AMD and RP) are associated with a decrease in OS length. One possible cause of decreased OS length is *mitochondrial inefficiency*, or inefficiency in *OS*

energy utilisation. This may be represented in the model by decreasing the IS ATP production rate or increasing the ATP threshold. Both changes decrease OS length, suggesting that these factors are sufficient to explain the OS shrinkage observed in diseased states. The above inefficiencies could also be represented by increasing the rate at which the ISs take up oxygen or reducing the oxygen threshold; however, this has an insignificant effect on OS length, since, although it decreases the steady-state OS length, the steady-state is not reached during a standard diurnal cycle.

The above study illustrates the way in which mathematical models can be used to isolate mechanisms in a way that would be difficult, if not impossible, experimentally; examining their sufficiency in explaining observed behaviours. Future models could incorporate the effects of Ngb in oxygen transport (see Section 3.2), or signalling between the photoreceptor and the RPE (Macdougall, 2015). The model could also be developed to consider disease states. For example, it could be combined with the oxygen toxicity mode for RP, described in Section 5.1.3, to account for the increased oxidative damage incurred by the IS as they approach the choroid, following shrinkage of the OS.

4. Development

4.1. Retinal Angiogenesis

The retinal capillary layers, also known as the *retinal vascular plexus* (RVP), colonize the retina via the process of *angiogenesis* (the development of new blood vessels from pre-existing vessels). *Astrocytes* migrate from the optic nerve, over the surface of the inner retina, in response to a gradient in *platelet-derived growth factor A* (PDGF-A), which is produced by the underlying retinal ganglion cells. Astrocytes in turn guide the formation of the RVP, producing *vascular endothelial growth factor A* (VEGF-A), which attracts *endothelial cells* to move up spatial gradients in its concentration, from the optic nerve, toward the retinal periphery. Astrocyte migration begins shortly before birth, whilst endothelial migration begins on *post-natal day* 0 (P0), reaching the retinal periphery by P8 (Aubert et al., 2011; McDougall et al., 2012; Watson et al., 2012).

Aubert et al. (2011); McDougall et al. (2012) and Watson et al. (2012) have created a series of models, produced alongside an accompanying experimental program, to capture the dynamics of the angiogenesis of the superficial RVP, in the developing murine (mouse) retina. The mammalian retina is an ideal system for studying angiogenesis, since the vascular architecture can easily be imaged using *retinal whole mounts*. Furthermore, development can be split into a well-defined sequence of events and the vessel network has an ordered architecture, facilitating comparisons between *in vivo* and *in silico* results.

In Aubert et al. (2011), two 1D PDE models are developed, defined on a domain spanning the region between the centre of the optic nerve and the position of the retinal periphery once fully-grown, starting from P0 (for model 1) or E17 (*embryonic day* 17, or P-4, for model 2) and running to P8. The first model focusses on capillary tip density, blood capillary density (which follow behind the capillary tips) and VEGF-A concentration, whilst the second accounts also for astrocyte density and PDGF-A concentration.

In the first model, an initial VEGF-A gradient is imposed, whilst in the second, the VEGF-A gradient is initially set to zero, and evolves over time as it is produced by astrocytes and consumed by endothelial cells, matching the *in vivo* situation more closely. Sensitivity analysis of the first model shows that *chemotaxis* has a significant influence upon RVP development, confirming the importance of the more realistic chemotactic gradients in the second model. The simulation predictions for capillary tip and astrocyte migration from the second model are in good agreement with the *in vivo* results, providing experimental support for the model and showing that the factors accounted for in the model are sufficient to explain the observed dynamics.

In later work, a 2D *hybrid model* (containing both discrete-stochastic and continuous-deterministic elements), posed on a domain spanning the surface of the inner retina, was used to simulate the complex, branched structure of the RVP (McDougall et al., 2012; Watson et al., 2012). As before, PDEs are defined for the astrocyte and endothelial cell densities (the distinction between capillary tips and blood capillaries being dropped at the level of the PDEs) and for the PDGF-A and VEGF-A concentrations. Four additional PDEs are also included to account for the density of the matrix-bound proteins *vitronectin* and *fibronectin*, both of which are produced by astrocytes, and the concentrations of astrocyte and endothelial cell produced *matrix degrading enzymes*, which degrade vitronectin and fibronectin respectively. Astrocytes and endothelial cells move up adhesion gradients in vitronectin and fibronectin respectively, via *haptotaxis* (see Figure 6(a)).

In order to capture the migration of individual astrocytes and endothelial cells, and hence the formation of discrete capillary vessels, the PDEs for these equations are discretized (so that these quantities are described at discrete points in space and time, rather than as a continuum). The direction of movement of each individual cell is determined stochastically (randomly), integrating the effects of *diffusion* (random movement), chemotaxis and haptotaxis. Both astrocytes and endothelial cells also undergo stochastic branching, the probability of *branching* increasing with increasing PDGF-A and VEGF-A concentrations respectively, whilst *anastomoses* occur whenever a sprout tip meets either another sprout tip or an existing capillary.

Blood is a *biphasic* fluid, composed largely of erythrocytes and plasma. The model accounts for the separation of these two phases at bifurcations in the vascular bed. The model also accounts for changes in vessel radius due to wall shear stress, intravascular pressure, *conducted* (acting upstream) and *convected* (acting downstream) *metabolic stimuli* and a shrinking tendency which dominates in the absence of growth stimuli. The conducted and convected stimuli help to prevent *shunt formation* by favouring the dilation of vessels that are part of extended flow pathways.

Lastly, the model contains PDEs to describe the oxygen dynamics in the tissues and within the blood vessels. It is also assumed that erythrocytes are the only source of oxygen. *Vessel*

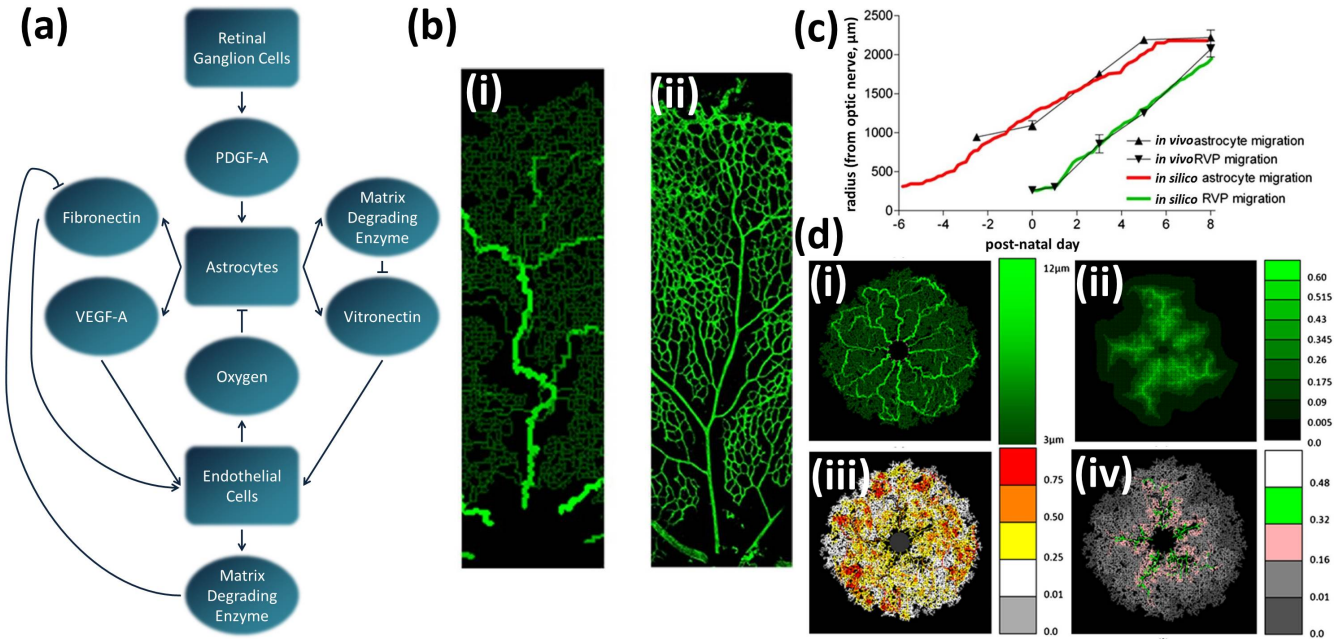

Figure 6: McDougall and co-workers' hybrid model of retinal angiogenesis (McDougall et al., 2012; Watson et al., 2012). (a) diagram summarising the key components and processes included in the model. Pointed arrows indicate production or attraction, whilst flat-headed arrows represent degradation or inhibition. Figure adapted from McDougall et al. (2012). (b) comparison between *in silico* (i) and *in vivo* (ii) vasculatures at P7.7 and P8 respectively (using the full model). Brighter colour in the *in silico* image represents wider vessels, corresponding with the colour bar in (d)(i). The results are qualitatively similar, the main differences being that, *in silico*, the vascular plexuses are slightly denser and the vessels remain dilated up to the growth front, rather than narrowing toward the periphery. Figure reproduced, with permission, from Watson et al. (2012). (c) graph comparing the *in vivo* and *in silico* (neglecting perfusion) migration of astrocyte and endothelial cell fronts. The *in vivo* results are represented by black triangles (upward: astrocytes, inverted: endothelial cells), whilst the *in silico* results are represented by red (astrocytes) and green (endothelial cells) lines. The results show good agreement. (d) simulation results from the full model at P7.7 showing (i) vessel radii, (ii) tissue oxygen concentration, (iii) haematocrit and (iv) vessel oxygen concentration. Figures (c) and (d) reproduced, with permission (and modifications in (c)), from McDougall et al. (2012). PDGF-A: platelet-derived growth factor A, VEGF-A: vascular endothelial growth factor A, P: post-natal day, RVP: retinal vascular plexus.

pruning occurs when the oxygen concentration in the surrounding tissue and vessel age exceed critical thresholds and in the absence of any flow-related stimuli.

Simulations including astrocyte and endothelial cell migration, but neglecting perfusion, produce cell front migratory dynamics that match well with *in vivo* experiments (see Figure 6(c)); however, they do not reproduce the highly structured vascular trees seen in vivo. When perfusion, plexus remodelling and oxygen delivery, without convected and conducted stimuli, are included, capillary shunts develop, such that the *haematocrit* only takes non-zero values in the regions neighbouring the optic nerve. As a result, oxygen delivery to the peripheral retina is negligible. When convected and conducted stimuli are included (see Figure 6(d)), the haematocrit is spatially heterogeneous, and the entire retina receives a reasonable supply of oxygen, demonstrating the importance of these stimuli for adequate oxygen delivery. Interestingly, the haematocrit is predicted to increase toward the retinal periphery, exceeding 0.75 in some regions around the periphery (this is as compared with the input value of 0.45), in good agreement with Ganesan et al. (2010a) (see Section 3.1) and being most highly concentrated around dilated arterio-venous loops. This phenomenon is due to *phase separation* (the separation of erythrocytes from plasma), which causes the haematocrit to increase along the arterial side of each bifurcation. In the absence of phase separation, the peripheral retina would be oxygen starved. Also in agreement with Ganesan et al. is the development of arterial inlet segments that are narrower than those of the venous outlet segments. Visual comparison of *in vivo* and *in silico vascular architectures* reveals that they are qualitatively similar, the main differences being that *in silico*, the vascular plexuses are a little denser and the vessels remain dilated up to the growth front, rather than narrowing toward the periphery (see Figure 6(b)).

Having benchmarked their model against normal development, it can be used to predict what would happen if one or more developmental mechanisms were altered. For example, increasing or decreasing the VEGF-A diffusion coefficient 10-fold slows the rate of capillary growth, due to the loss of sharp gradients in VEGF, suggesting that the usual *isoform* (VEGF-A_{164}) is more effective for retinal angiogenesis that its lighter and faster diffusing (VEGF-A_{120}), and its heavier and slower diffusing (VEGF-A_{188}) isoforms.

Increasing the input arterial haematocrit, or decreasing the tissue oxygen consumption rate causes large capillary-free zones and hyperoxia to develop, these effects being more extensive in the latter case. The former case is equivalent to *retinopathy of prematurity* and the latter to *oxygen-induced retinopathy*.

If capillary pruning is reduced, the spatial distribution of dilated vessels is not significantly affected, but phase separation is reduced, causing haematocrit levels across the retina to be-

come more heterogeneous, with erythrocytes being more concentrated around the dilated arteriolar segments. These results suggest that capillary pruning is important in ensuring that all regions of the retina receive an adequate supply of oxygen.

The above results illustrate how computational models can be used to examine scenarios and isolate mechanisms in a way that would be technically challenging, if not impossible, to reproduce experimentally. This is particularly true for the simulations in which the convected and conducted stimuli are switched off.

Extending the hybrid mode to 3D would allow studies of later developmental stages (between P8 and P16), during which vertical sprouting from the superficial RVP leads to the formation of two additional RVP layers deeper within the retinal tissue (McDougall et al., 2012; Watson et al., 2012). This would require a fully 3D model. It would also be interesting to test whether the model could be adapted to account for the curved vascular arcades seen in humans (as opposed to the radial pattern found in the murine retina). The effects of mechanical signalling upon vessel formation and maturation could also be incorporated. Lastly, the model could be adapted to study *diabetic retinopathy* and the *critical developmental period* in the early stages of RP (Mervin and Stone, 2002), providing a tool for testing potential treatment strategies.

Finally, we note that recent modelling studies have also considered angiogenesis within the (normally avascular) cornea, where angiogenesis is induced either by inserting a pellet containing angiogenic factor into the cornea or by cauterizing the cornea to induce inflammation (see, Connor et al., 2015; Jackson and Zheng, 2010). The visibility and normally avascular nature of the cornea make it a useful experimental model for angiogenesis in other contexts, such as in tumours.

4.2. Retinal Mosaic Formation and Retinogenesis

A number of theoretical modelling studies have explored the formation of retinal photoreceptor and ganglion cell *mosaics*, using a combination of phenomenological and mechanistic approaches. Typically focussing on the processes of lateral migration, cell fate and cell death, these studies seek to explain how a regular arrangement of neurons emerges from an initially random distribution. These studies are reviewed in detail in Eglen (2006, 2012), to which the reader is referred for further details.

More recently, Salbreux et al. (2012) have developed a computational model to explain the ordered packing of cone photoreceptors in the zebrafish retina, in terms of the coupling of mechanical deformations and planar cell polarity. Their model reproduces many behaviours observed during development *in vivo*, as well as elucidating how this process may break down in mutants. In addition, Jiao et al. (2014) have constructed a multiscale (spanning multiple spatial scales) model for the packing of avian photoreceptors. The model indicates that short- and long-range repulsive forces between photoreceptors are sufficient to explain the observed patterns.

Barton and Fendrik (2015) have used a stochastic model to explore vertebrate *retinogenesis*, the process by which different retinal cell types derive from multipotent retinal progenitor cells. The model, which assumes that a single factor regulates both division and competency, reproduces the timings at which different cell types are produced, as measured in rats, suggesting that a single regulatory factor is sufficient to explain this process.

5. Disease

The various diseased and damaged states of the retina have received a significant proportion of the theoretical modelling community's attention. Models cover a range of topics including laser-induced damage (Till et al., 2003), blast injury (Rossi et al., 2012), retinal detachment (Jiann et al., 2015; Meskauskas et al., 2012), proliferative retinopathy (Maggelakis and Savakis, 1996, 1999), retinitis pigmentosa and age-related macular degeneration. In what follows, we focus on the latter two conditions, where modelling studies are most highly concentrated.

5.1. Retinitis Pigmentosa

The term *retinitis pigmentosa* (RP) denotes a group of inherited retinal diseases which cause the progressive degeneration of photoreceptors and, hence, loss of vision. The most common inherited retinal degeneration, RP is currently untreatable (Shintani et al., 2009). RP usually occurs as a *rod-cone dystrophy*, in which rod function and number are diminished earlier and more severely than for cones (Hamel, 2006). *Cone-rod dystrophies*, in which cone loss precedes rod degeneration, can also occur and, rarely, rod and cone loss may occur *simultaneously* (Hartong et al., 2006). Whilst the initial loss of rods (or cones) may be attributed to genetic mutations, the cause of the secondary loss of cones (or rods) is unknown.

Histological studies in humans and rats suggest that photoreceptor degeneration initiates in *patches*, which presumably spread and coalesce over time (Cideciyan et al., 1998; García-Ayuso et al., 2013; Ji et al., 2012; Lee et al., 2011; Zhu et al., 2013). RP progression in animal models is largely homogeneous in space; however, in humans, photoreceptor loss has a distinct *spatio-temporal pattern*, typically initiating in the mid-periphery, with the central retina being the last region to degenerate (Hartong et al., 2006). While the phenomena driving this pattern remain to be determined, three hypotheses have been proposed to explain them: the *trophic factor*, *toxic substance* and *oxygen toxicity hypotheses*. Mathematical modelling has proven valuable in evaluating the strengths and weaknesses of these hypotheses and in suggesting potential treatment strategies.

5.1.1. The Trophic Factor Hypothesis

It has been suggested that rods may release chemicals that are essential for cone survival (Fintz et al., 2003; Mohand-Saïd et al., 1998, 2000, 1997). Rod loss would remove the source of these factors, leading to cone degeneration. One such factor, *rod-derived cone viability factor* (RdCVF), identified by Léveillard et al. (2004), has been shown to slow cone degeneration and to preserve cone function in chick, mouse and rat models (Fintz et al., 2003; Léveillard et al., 2004; Mohand-Saïd et al., 1998, 2000, 1997; Yang et al., 2009).

Camacho, Wirkus *et al.* have developed a series of *spatially-averaged* ODE models to investigate the role of RdCVF in both the healthy and diseased retinas (Camacho et al., 2010, 2014; Camacho and Wirkus, 2013; Colón Vélez et al., 2003).

Their first model considers the healthy retina. It consists of 3 ODEs, describing the dynamics of rod and cone OS number, and RPE cell number (equivalent to the trophic pool, Camacho et al., 2010, note that we use the interpretation given in the subsequent papers). Their equations describe the shedding and renewal of the rod and cone OSs, where the renewal involves the conversion of trophic pool (which is continuously replenished) into new OS discs. Rods produce RdCVF, which is mathematically distinct from the trophic pool, at no cost to themselves (that is, without affecting the rate of rod OS shedding and renewal), augmenting the supply of trophic factor to the cones and thus increasing the rate of cone OS renewal (see Figure 7(a)). The presence of RdCVF makes it possible for rods and cones to coexist indefinitely, suggesting that this factor may be necessary for their mutual survival (Camacho et al., 2010). We note that earlier modelling work by Camacho and colleagues (Colón Vélez et al., 2003) and experimental work by Mohand-Saïd and colleagues (Mohand-Saïd et al., 1998, 1997) predicted the existence of such a factor, before its discovery by Léveillard et al. in 2004.

Mathematical analysis and numerical simulations suggest that, for certain parameter values, the system will exhibit multiple *stable oscillatory solutions*, of various amplitudes, corresponding to the rhythmic shedding and renewal of photoreceptors observed *in vivo* (see Figure 7(b)). A solution is said to be *stable* if the system always returns or remains close to it following a small perturbation and is *unstable* otherwise. Outside this parameter range, rods, cones and RPE cannot coexist. Within this parameter regime, the period of oscillation ranges from 8–9 hours, for small amplitude oscillations, to 26 hours, for large amplitude oscillations. This oscillatory behaviour is more robust (that is, it is more likely to occur and to be maintained) when rods produce RdCVF at a faster rate and when photoreceptors convert trophic factor into OS more efficiently.

The model further predicts that rod and cone OS lengths oscillate *in phase* (in synchrony). This has been observed *in vivo*, but is not true of all species (see Camacho et al., 2010, and references therein). It would be interesting to investigate ways in which the model might be modified to induce *out-of-phase* (asynchronous) oscillations, for example, by introducing an *explicit time delay* in the aid supplied to the cones via RdCVF, capturing the *in vivo* delay (Camacho et al., 2010).

Camacho and Wirkus (2013) extended their model to describe the disease state of RP by distinguishing between *normal* and *mutant rods*, where both types of rod are genotypically mutant, but only the latter type has had its functionality compromised (represented in the model by altered rates of shedding and renewal of OS). Normal rods can become mutant, but not vice versa, whilst both normal and mutant rods consume trophic factor and contribute RdCVF to the cones. The RPE equation is also modified so that, neglecting the terms involving photoreceptors, it obeys logistic (such that RPE cell numbers approach a finite 'carrying capacity' over time), rather than exponential (where RPE cell numbers increase unboundedly, at a rate proportional to the current number of RPE cells) dynamics, the number of RPE cells remaining bounded under all conditions (see Figure 7(a)).

Mathematical analysis reveals that, for any given set of parameter values, there exist seven *equilibrium* (steady-state) *solutions*, each corresponding to a different stage in the disease progression, from healthy to completely degenerate. Numerical simulations suggest that only one of these equilibrium solutions is stable for any biologically realistic parameter set and that the system will settle at the stable equilibrium solution. Four parameters, which are key in determining the form of the disease progression, are identified, namely the *ratios of shedding rates to renewal rates* in normal rods, mutant rods and cones, and the *carrying capacity* of the RPE (the maximum number of RPE cells that can be supported by the system in the absence of photoreceptors). All of these parameters must remain fixed in order for an equilibrium solution to remain stable, whilst changes in parameter values can drive disease progression between the different equilibrium solutions.

The system switches between equilibrium solutions via *transcritical bifurcations*, at which a change in parameters causes a pair of equilibrium solutions, one stable and the other unstable, to momentarily meet and exchange stability. As this happens, the system transfers from the first equilibrium solution, which is now unstable, to the second equilibrium solution, which is now stable. Variation of parameters allows a variety of paths to be traced to total blindness, passing through different combinations of equilibrium solutions, corresponding either to the rod-cone, cone-rod or simultaneous form of RP (see Figure 7(c)).

The above results suggest potential *therapeutic strategies*, that could halt disease progression. For example, the model predicts that progression of rod-cone RP requires a decrease in the ratio of shedding to renewal in cones. Therefore, a treatment designed to maintain this ratio might prevent disease progression in patients whose rods and cones are degenerating via this pathway.

This model generated two other, noteworthy results. Firstly, small changes in parameter values can lead to markedly different pathways to blindness, helping to explain the differences in disease progression seen in closely related patients with the same mutation. For example, an increase in the ratio of shedding to renewal in cones can change the disease progression from one in which all photoreceptors are lost simultaneously, to one in which cones are lost before rods. Secondly, the model suggests that the reduction in photoreceptor OS length observed in RP is an *emergent property* (a system-level behaviour that arises through lower-level interactions between elements within the system) of the nonlinear interactions between rods, cones and RPE, rather than simply due to changes in shedding and renewal rates.

Lastly, Camacho et al. (2014) modified their RP model to include an RdCVF treatment term (see Figure 7(a)). Using *optimal control theory*, they determined a treatment level that will achieve the desired degree of cone preservation, whilst minimising the RdCVF dose. This is important, since using too large a dose of RdCVF could impair retinal function. A

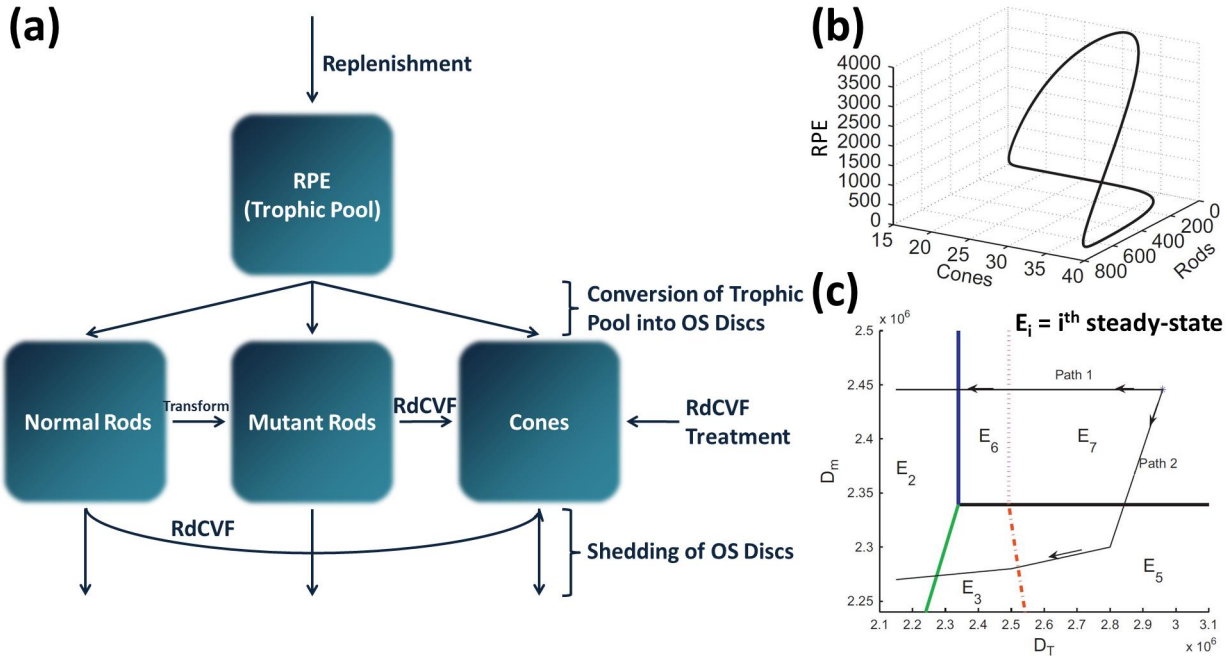

Figure 7: Camacho and Wirkus *et al.*'s trophic factor model of RP. (a) diagram showing the components and processes in the Camacho et al. (2014) model. (The Camacho and Wirkus (2013) model does not include RdCVF treatment, whilst the Camacho et al. (2010) model includes neither treatment, nor the mutant rod component and its associated processes.) Figure adapted from Camacho et al. (2010) and Camacho and Wirkus (2013). (b) *stable limit cycle* (oscillatory) solution of the Camacho et al. (2010) model, demonstrating the rhythmic shedding and regrowth of rod and cone OS in the healthy retina. Figure reproduced, with permission and modifications, from Camacho et al. (2010). (c) diagram showing two alternative paths (marked with arrows) that may be traced through parameter space, leading to different cone-rod dystrophy forms of the RP disease progression, in the Camacho and Wirkus (2013) model. Lines without arrows demarcate the boundaries of the stability regions, across which (transcritical) bifurcations occur. Path 1: $E_7 \rightarrow E_6 \rightarrow E_2$. Path 2: $E_7 \rightarrow E_5 \rightarrow E_3 \rightarrow E_2$. D_m: ratio of shedding rate to renewal rate in mutant rods, D_T: RPE (trophic pool) carrying capacity, E_7: healthy steady-state, E_6: steady-state at which all cones are lost, E_5: steady-state at which all normal rods are lost, E_3: steady-state at which all cones and normal rods are lost, E_2: steady-state at which all photoreceptors are lost. Figure reproduced, with permission and modifications, from Camacho and Wirkus (2013).

two week treatment period is considered for comparison with Léveillard et al.'s (2004) experimental results. Simulations, starting from different stages in the disease progression, reveal that treatment will have a negligible effect on rod loss, but can significantly reduce cone loss during the later stages of the disease (when all the rods have been lost), provided the treatment is aggressive enough. It is also possible, using the model, to estimate the minimum treatment required to achieve the approximate 40% sparing of cones reported in Léveillard et al. (2004).

5.1.2. The Toxic Substance Hypothesis

Another mechanism by which photoreceptor cell death could spread is via the release of toxic substances by dying photoreceptors. These substances are most likely released into the interphotoreceptor matrix, where they are taken up by and, thus, poison neighbouring photoreceptors. It has been suggested that toxic substances may be transmitted between photoreceptors via gap junctions; however, this hypothesis is now in doubt, since disruption of gap junctions does not seem to affect disease progression (Kranz et al., 2013; Ripps, 2002).

Clarke et al. (2000) have suggested a *one-hit model* of neuronal cell death, where the time at which a neuron dies is random, for a variety of conditions including RP (see also Clarke and Lumsden, 2005a,b; Clarke et al., 2001). This model arises from experimental observations which suggest that the risk of (photoreceptor) cell death is either constant or decreases exponentially with age (Clarke et al., 2000).

This model can be justified at the biochemical level by the *mutant steady-state* (MSS) *hypothesis*, which suggests that mutations result in elevated levels of a pre-apoptotic compound, placing it closer to a critical threshold, above which apoptosis is induced (Clarke et al., 2001). Random fluctuations in the concentration of this compound may cause it to exceed this threshold, resulting in cell death (Clarke et al., 2001).

Burns et al. (2002) incorporated the MSS hypothesis into a 1D spatial model, consisting of a pair of PDEs, in which a diffusible *toxic factor*, produced by dying photoreceptors and released into the interphotoreceptor matrix, upregulates the production of *pre-apoptotic factors* in the surrounding photoreceptors. Assuming that the rate of toxic factor uptake is linear (that is, directly proportional to the toxic factor concentration), the toxic factor PDE can be solved analytically, so that the problem reduces to solving a single PDE for the pre-apoptotic factor. Since the pre-apoptotic factor is unable to move between photoreceptors, its PDE lacks terms for diffusion or transport, containing only kinetic (reaction) terms. Thus, it may be split into N spatially dependent ODEs, one for each of the N photoreceptors spanning the domain, where the ODEs' spatial dependence

arises through their dependence upon the toxic substance concentration.

In the absence of toxic factor, each of the ODEs is *bistable*, such that the pre-apoptotic factor concentration can exist stably at either of two steady-state values (see Figure 8(a)). The solution with the lower value (zero) corresponds to the MSS, in which all photoreceptors are assumed to start, whilst the upper (strictly positive) value corresponds to the state in which a photoreceptor is committed to apoptosis. These two stable steady-states are separated by an unstable steady-state. Increases in the concentration of the toxic factor above a *critical threshold* cause the lower stable and unstable steady-states to approach one another, coalesce and annihilate, such that the upper stable steady-state becomes the attractor for the whole system. That is to say, for any given starting point, the system will move towards this steady-state. Provided the toxic factor concentration remains elevated for long enough, the system will become irreversibly trapped in this steady-state's basin of attraction (such that it continues to move towards the steady-state), at which point the photoreceptor is considered to be *committed to apoptosis*.

A stochastic simulation algorithm is used to determine when a photoreceptor in the commitment state will undergo apoptosis, where the lifetime of each photoreceptor in the commitment state is drawn from either a normal or an exponential distribution. Upon apoptosis, a photoreceptor releases toxic factor into the extracellular space where it evolves over time according to the analytical (algebraic) solution to its associated PDE. The degeneration process is initiated by selecting a single photoreceptor to undergo apoptosis. When the lifetime in the commitment state is normally distributed, the decline in photoreceptor number is slow and sigmoidal (with an 'S' shaped profile). However, when it is *exponentially distributed*, photoreceptors are lost more rapidly, declining exponentially, in agreement with the experimental studies mentioned above (Clarke et al., 2000, 2001). This suggests that photoreceptor lifetimes in the apoptosis commitment state are exponentially, rather than normally, distributed. Simulations also demonstrated that when multiple photoreceptors undergo apoptosis at points that are close in space and time, the released toxic factors may have a *synergistic* effect, committing more photoreceptors to apoptosis than would occur if the initial releases of toxic factor had been more distantly separated in space and/or time (see Figure 8(b)).

The model also predicts a *patchy pattern* of photoreceptor loss, similar to that often observed in the early stages of RP (see above), with patch diameters similar to those seen *in vivo*, providing a potential explanation for these patterns (see Figure 8(c)).

More recently, Lomasko et al. (2007a,b) and Lomasko and Lumsden (2009) have extended the work of Burns et al. (2002) by constructing stochastic models of cytoskeleton-induced neuron death. While these models were not developed specifically for the retina, it is noteworthy that they replicate the exponential and sigmoidal patterns of cell loss measured by Clarke et al. (2000).

5.1.3. The Oxygen Toxicity Hypothesis

The final hypothesis suggests that the initial loss of photoreceptors results in a rise in oxygen levels, due to decreased demand, creating a toxic environment for those that remain (Stone et al., 1999; Travis et al., 1991; Valter et al., 1998). These oxygen levels are maintained, since the CC, which is the main source of oxygen for the photoreceptor containing outer retina, autoregulates poorly in response to hyperoxia (Stone et al., 1999; Yu et al., 2004; Yu and Cringle, 2005). An increase in oxygen levels above normal physiological levels is harmful to retinal tissue, since it upsets the redox potential, resulting in increased production of *reactive oxygen species* which cause damage to lipids, protein and DNA (Ames et al., 1993, 1995; Kohen and Nyska, 2002; Shen et al., 2005).

Roberts (2015) has created a series of models examining the *oxygen toxicity hypothesis*. The models are formulated as systems of PDEs, for oxygen concentration, photoreceptor density (or rod and cone densities taken separately) and capillary (CC) surface area per unit volume. The models incorporate the heterogeneous distribution of rods and cones, whilst a spherical polar coordinate system (in which the coordinates are specified in terms of the distance from the origin, r, the polar angle, θ, and the azimuthal angle, ϕ) is used to capture the geometry of the eye. For simplicity, the retina is assumed to be symmetric in the azimuthal direction (for rotations about the axis, passing at a right-angle to the wall of the eye, through the foveal centre) and hence the optic disc is neglected. Oxygen supplied by the CC diffuses freely across the domain and is consumed by photoreceptors at a rate proportional to their density, whilst photoreceptors either remain at or approach their healthy local density under normoxia (unless they are absent, in which case their density remains at zero), but decay exponentially when local oxygen levels rise above a defined *hyperoxic threshold*. The CC dynamics follow those of the photoreceptors; however, since their rate of decay and regrowth is generally slower than that of the photoreceptors, their dynamics lag behind those of the photoreceptors.

The first set of models are posed on a 1D domain, spanning the region between the centre of the fovea and the ora serrata. Numerical solution and mathematical analysis of the steady-state 1D problem without capillary loss reveals the conditions under which a patch (corresponding to an annulus in 2D) of photoreceptor degeneration will spread or remain stationary. It is found that the retina may be divided into a series of 5 concentric *stability regions*, centred on the fovea (see Figure 9(a)). Starting from the centre of the retina these regions are: the central unstable region, the near-central stable region, the para/perifoveal unstable region, the mid-peripheral stable region and the peripheral unstable region. Wide patches (with width greater than about one-hundredth of the width of the domain) remain stationary, provided both boundaries lie within a stable region, and will expand otherwise. Therefore, provided a patch can be classified as wide, its stability properties do not depend upon its width, only the position of its boundaries. Narrow patches (with width less than about one-hundredth of the width of the domain, that is, less than about 40 photoreceptors across)

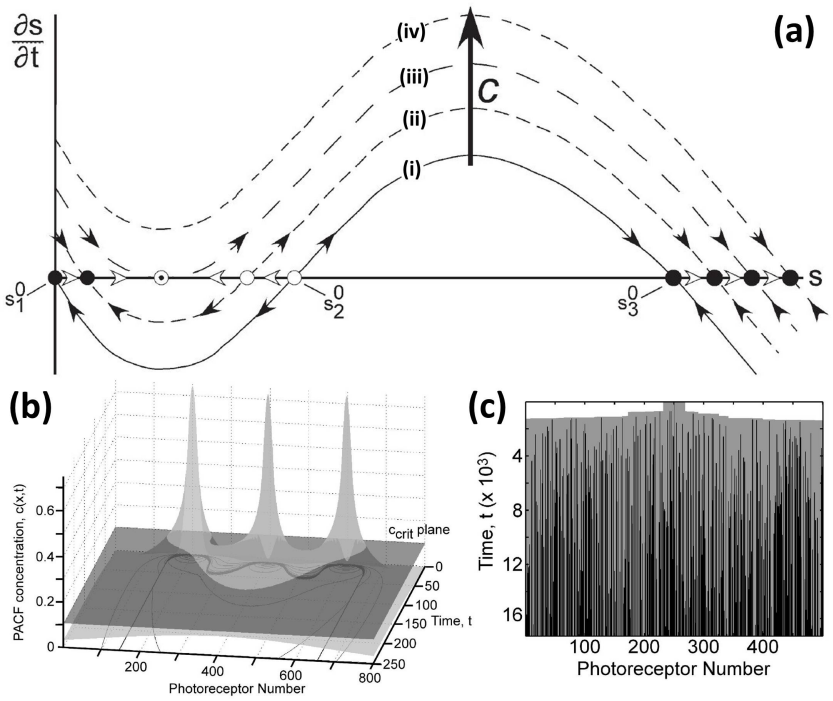

Figure 8: Burns et al.'s toxic substance model of RP. (a) graph showing how the time rate of change of pre-apoptotic factor concentration, $\partial s/\partial t$, evolves with increasing PACF (photoreceptor apoptosis commitment factor), c, concentration. When $c = 0$ (i), the system has three steady-states; two stable steady-states, s_1^0 (corresponding to the MSS) and s_3^0 (corresponding to the apoptosis commitment state), separated by an unstable steady-state, s_2^0. As c increases past c_{crit} (iii), s_1^0 and s_2^0 meet and annihilate, such that only s_3^0 remains for $c > c_{crit}$ (iv). When the system becomes irreversibly trapped by s_3^0's basin of attraction, it is considered to be committed to apoptosis. (b) graph showing the recruitment of photoreceptors to apoptosis, following three bursts of PACF release, at close points in space and time. PACF is released at $(x, t) = (200, 0)$, $(400, 10)$ and $(600, 5)$. The light grey surface shows the evolution of PACF concentration in space and time, whilst the dark grey surface is the $c(x, t) = c_{crit}$ plane. The black curve on the $c(x, t) = 0$ plane delimits the photoreceptors which have committed to apoptosis. The PACF bursts act synergistically, such that more photoreceptors are recruited to apoptosis than in the case where the bursts are more distantly separated in space and time. (c) stochastic simulation in which photoreceptors in the apoptosis commitment state undergo apoptosis after a time drawn from an exponential distribution. Upon undergoing apoptosis, a photoreceptor releases a burst of PACF, committing neighbouring cells to apoptosis. Grey regions represent photoreceptors committed to apoptosis and black regions represent photoreceptors which have undergone apoptosis. The recruitment cascade is initiated by a single PACF burst at $(x, t) = (250, 0)$. The results demonstrate a patchy loss of photoreceptors, similar to that which is often seen in the early stages of RP. Figures reproduced, with permission (and modification in (a)), from Burns et al. (2002).

are stationary within the 'stable' regions, and are also stationary within 'unstable' regions, provided they are sufficiently narrow.

Simulations of the dynamic (time-dependent) 1D problem without capillary loss and with an initial patch of photoreceptor loss, together with mathematical analysis, reveal that the *wave speed* of photoreceptor degeneration is a decreasing function of the photoreceptor density local to the degenerating wavefront. This prediction awaits experimental/clinical confirmation.

Numerical solution and mathematical analysis of the steady-state 1D problem including capillary loss, reveals the counter-intuitive result that a patch of capillary loss must be essentially coincident with a patch of photoreceptor loss in order to stabilise it, in those cases where it would otherwise be unstable (given the assumption that the capillary loss does not extend beyond the degenerate photoreceptor patch). This is surprising, as it would have been natural to assume that a substantial region of capillary loss, within a patch of photoreceptor loss, would be sufficient to prevent further hyperoxia-driven photoreceptor degeneration. However, the above result suggests that this is not the case. This prediction could be tested experimentally in an animal model by using a laser to ablate the choroid within a patch of photoreceptor loss and also suggests a potential treatment strategy to arrest the progression of the disease in humans.

Dynamic simulations including capillary loss in 1D demonstrate that capillary loss may prevent, halt, delay or partially reverse (in the sense of restoring photoreceptor vitality, given that new photoreceptors cannot be generated) photoreceptor loss. Further experimental work is required to quantify the rate of CC degeneration and hence to determine its effect on photoreceptor degeneration.

The second set of models extends the previous models to 2D, spanning the region between the centre of the fovea and the ora serrata, whilst assuming that the capillary density remains constant. Simulations of the dynamic 2D problem demonstrate the *spatio-temporal patterns* of degeneration that the oxygen toxicity hypothesis can give rise to. In addition to the initial removal of annulus and disc shaped patches of photoreceptors, the hyperoxia-independent *mutation-induced* degeneration of either rods and/or cones is also included in some simulations, to represent the rod-cone, cone-rod and simultaneous forms of

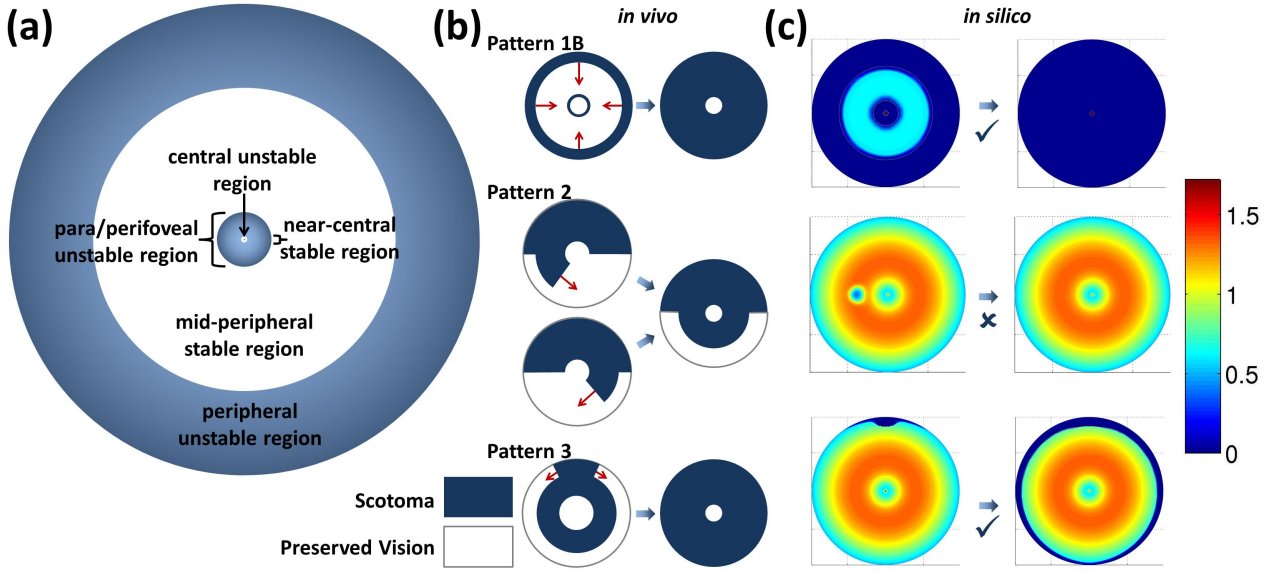

Figure 9: Roberts' oxygen toxicity model of RP. (a) diagram to show the arrangement of stable and unstable regions within the retina. (b) diagrams to show some of the *in vivo* patterns of visual field loss. Scotomas (blind spots) are shaded and areas of preserved vision are shown in white. (c) *in silico* results. Graphs show the photoreceptor density at earlier (left) and later (right) stages (the calibration of the heat map is given by the colour bar on the right, where 1 corresponds to 1.11×10^5 photoreceptors/mm^2). The problem is solved on a spherical surface and projected onto the x-y plane for visualisation. Pattern 1B and the later stage of pattern 3 are replicated; however, pattern 2 cannot be replicated (in the example shown, a partially degenerate disc recovers fully, in the sense of regaining vitality), the retina being resistant to the spread of photoreceptor degeneration in the mid-peripheral stable region. Figures reproduced, with permission and modifications, from Roberts (2015).

RP. The patterns formed are compared with those classified by Grover et al. (1998) in their study of visual loss in RP patients. Grover et al. identified three characteristic patterns or visual field loss: *pattern 1* involves concentric loss of visual field, sometimes accompanied by a perifoveal or parafoveal ring scotoma (blind spot); *pattern 2* begins with a nasal or temporal restriction, out from which an arcuate (bow shaped) scotoma winds through the mid-periphery; lastly, *pattern 3* starts with a mid-peripheral ring scotoma, which expands either temporally or inferiorly, leaving a U- or n-shaped peripheral visual field, the arms of which retract until peripheral vision is lost (see Figure 9(b)). In all cases, central vision is best preserved, though it is eventually lost unless preceded by patient mortality.

It is found that mutation-induced rod degeneration results in pattern 1 degeneration, including a para/perifoveal ring scotoma (see Figure 9(c)(top)), whilst patch loss in, or overlapping, the para/perifoveal region may also spread to form a para/perifoveal ring scotoma. Patch loss near the ora serrata spreads around the periphery of the retina, mimicking the latter stage of pattern 3 degeneration (see Figure 9(c)(bottom)). Mutation-induced cone loss results in degeneration of the central retina and may in some cases also result in degeneration of the peripheral unstable region. These results are consistent with the cone-rod dystrophy degeneration patterns described by Hamel (2007). It is not possible, with this model, to stimulate preferential loss from the middle of the mid-periphery associated with the intermediate stage of pattern 2 and the initial stage of pattern 3 (see Figure 9(c)(middle)). By isolating the oxygen toxicity mechanism, in a way that would not have been possible experimentally, these models highlight the strengths and weaknesses of this hypothesis. The replication of patterns seen *in vivo* demonstrates the sufficiency (though not the necessity) of this mechanism to generate certain patterns of degeneration, whilst the failure to replicate other patterns indicates that other mechanisms are likely to be at play here. This provides a useful insight for the development of future treatment strategies.

Both 1D and 2D models predict that treatment with *antioxidants* and/or *trophic factors* could prevent, halt, delay or partially reverse (in the sense of restoring photoreceptor vitality) photoreceptor loss, depending upon the strength and timing of the treatment. Since the analysis and simulations indicate that the para/perifoveal and peripheral unstable regions are the most susceptible to hyperoxic degeneration, this suggests that, if possible, treatment should preferentially target these regions.

A natural way to extend this modelling work would be to adapt the modelling framework, with its incorporation of the distribution of rods and cones, to consider the dynamics of disease progression under the trophic factor and toxic substance hypotheses. These models could perhaps explain the other observed patterns of photoreceptor loss in RP. The latter hypothesis has particular potential to explain the preferential loss of photoreceptors from the middle of the mid-periphery seen in progression patterns 2 and 3, as it is here that the toxin producing rods are most densely packed. This could then be followed by more comprehensive models which combine the three RP hypotheses. Following sufficient benchmarking, such models could be used to inform treatment decisions, parametrising the model to make it patient specific.

Perhaps the most useful data, for informing future modelling studies, could be derived from a detailed longitudinal clinical study, measuring the precise positions of the boundaries of degenerate photoreceptor, RPE and CC patches, at regular intervals throughout the disease progression, together with the rod and cone densities across the retina at each stage, in a range of patients. This could be done using optical coherence tomography and adaptive optics scanning light ophthalmoscopy (Liu et al., 2014; Murakami et al., 2008). Combining this with visual field tests, multi-focal electroretinograms and autofluorescence imaging would enhance these studies still further (Robson et al., 2006). This would yield better parametrised models, which have the potential to more accurately predict the pattern and speed of degeneration. Present studies tend to focus on the patterns of visual field loss, rather than changes in the photoreceptor density, making it difficult to determine precise measurements for the retinal locations affected. In addition, the early stages in the disease progression are often not recorded (largely because symptoms tend not to manifest until later in life) and the intervals between measurements are too long (it would be helpful if observations could be made on at least an annual basis).

5.2. Choroidal Neovascularisation

Choroidal neovascularisation (CNV) is a process which occurs during the advanced stage of neovascular (wet) AMD (Jager et al., 2008). It involves the growth and spread of the choroid past *Bruch's membrane* (BM), which in health forms a barrier between the choroid and the RPE, into the retina. The choroidal vessels penetrating the retina are abnormally permeable and fragile, leading to the build-up of fluid and subsequent damage to the retina. The physiological and biochemical mechanisms underlying CNV are not well understood, whilst present treatment strategies show limited success (Coleman et al., 2008).

Flower et al. (2001) have constructed a model which relates the blood flow in the CNV to that in the underlying CC. The CC is modelled as a (2D) planar porous medium, with a set of sparsely distributed inflows and outflows (arranged according to the histology of a sample human eye), which supply and drain blood from deeper within the choroid, whilst the CC is connected to the CNV via capillary-like vessels. The model predicts that reducing the blood flow in an arteriole/venule, feeding/draining the CC, by as little as 50% could be sufficient to significantly reduce or halt blood flow in an overlying CNV, whose penetrating vessels neighbour the arteriole/venule.

The model has clear implications for potential treatment strategies. Flower et al. (2001) suggest that it may be better to target the underlying choroid, rather than destroying the CNV, which often results in recurrence. At present, treatment only targets arterioles, whereas the model suggests that ablating venules could be just as effective. If the model could be tailored to individual patients, then it could potentially be used to determine which arterioles and venules to target, optimising treatment.

Shirinifard et al. (2012) have developed a 3D computational model of the choroid and outer retina in which they investigate the role played by *adhesion* in CNV progression. The model is of the *cellular Potts* type, where each model 'cell' is composed of a set of (simply) connected points on a pre-defined lattice. The model 'cells' may either represent biological cells, parts of cells or fluid-containing regions, their positions being updated stochastically over time, subject to energy (e.g. adhesion energies) and other constraints. The model accounts for vascular cells (of the CC), stalk cells (of the CNV), tip cells, RPE cells, photoreceptor OS cell parts, photoreceptor IS cell parts, BM, medium (which fills the spaces unoccupied by cells or BM), oxygen, VEGF and matrix metalloproteinases (MMP).

Each simulation begins either with or without a single *tip cell* (an endothelial cell which leads other endothelial cells upon activation of sprouting angiogenesis), which degrades the BM via the secretion of MMP, allowing it to penetrate the retina. In each case, the simulation time covers a year's disease progression, the first three months of which are regarded as the *early phase* and the last three months of which are denoted the *late phase*.

In both the early and late phases, one of three patterns of vascularisation may occur: *type 1* (sub-RPE) CNV, with a vascular layer between BM and the RPE; *type 2* (sub-retinal) CNV, with a vascular layer between the RPE and the photoreceptors; and *type 3* (combined pattern) CNV, which combines both of the above vascular layers. The model accounts for the adhesion between RPE cells and BM (RPE-BM), between neighbouring RPE cells (RPE-RPE) and between RPE cells and photoreceptor OSs (RPE-POS, see Figure 10(a)). All three pairings involve *labile adhesion* (without junctional structures), whilst the first two also involve *plastic coupling* (with junctional structures). The combination of these two types of adhesion is known as *junctional adhesion*. This gives rise to five adhesion parameters, corresponding to each of the adhesion types between each sort of structure. By varying these parameters, the effects of adhesion failure upon disease progression can be determined (see Figure 10(b)).

A total of six scenarios are observed, as judged by the pattern of vascularisation at the early and late phases: stable type 1 (early and late type 1), early type 1 to late type 2 (see Figures 10(c) and (d)), early type 1 to late type 3, stable type 2 (early and late type 2), early type 2 to late type 3, and stable type 3 (early and late type 3). It is found that the combination of the presence of a tip cell and the occurrence of adhesion failures are both necessary and sufficient for CNV to initiate, and that severe impairment of any one of the three adhesion pairings can independently induce CNV. In particular, reduced RPE-BM adhesion results in early type 1, reduced RPE-RPE or RPE-POS adhesion results in early type 2, and simultaneous reduction of RPE-RPE and RPE-BM results in either early type 1 or early type 2, which may often progress to late type 3. Simulations also reveal that the plastic coupling strengths have a relatively minor effect on the ability of the retina to resist CNV, with labile adhesion playing the most important role.

Many previous studies have suggested that CNV results either from the overexpression of VEGF or holes in BM (Shirinifard et al., 2012). Simulations demonstrate that overexpression of VEGF increases the probability of CNV initiation, but that the early and late vascular patterns do not change, whilst holes

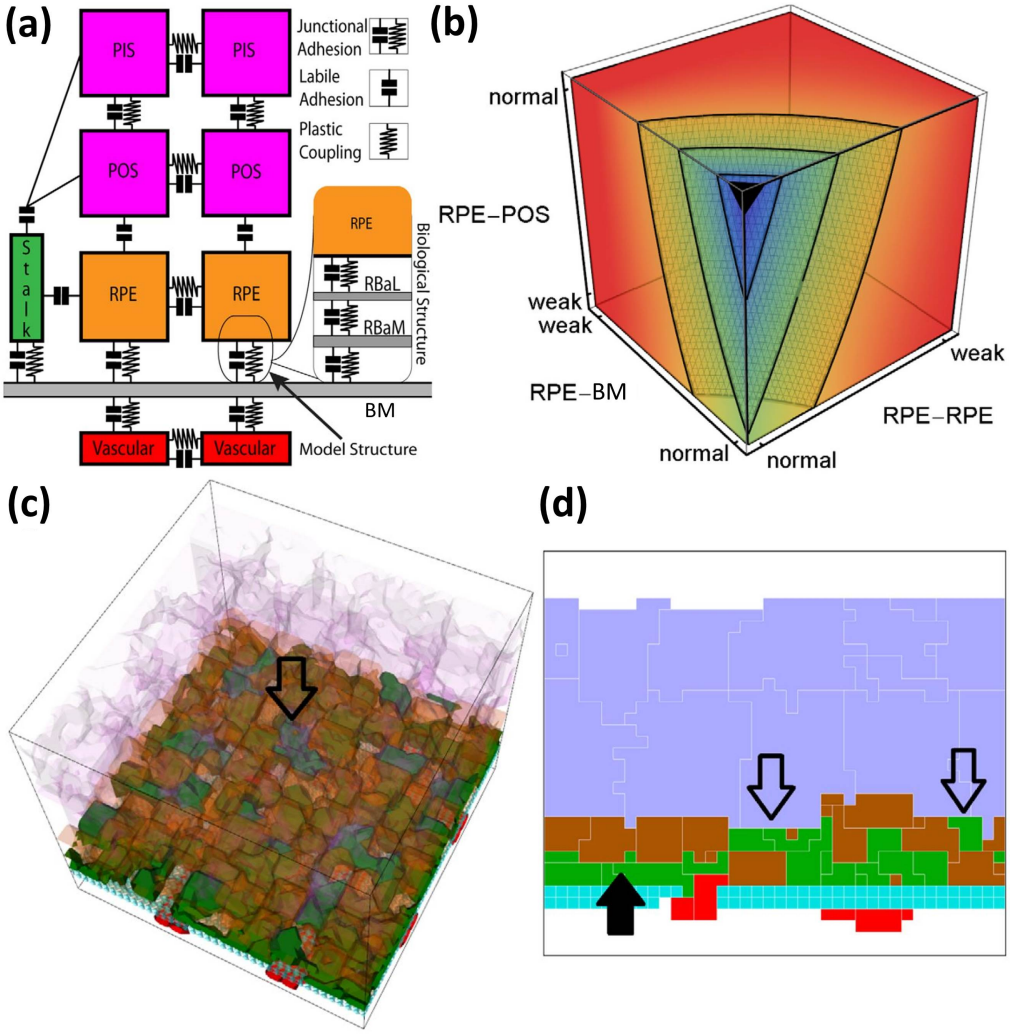

Figure 10: Shirinifard et al.'s model of CNV. (a) diagram showing the adhesive coupling between retinal components. Plastic coupling involves junctional structures, whilst labile adhesion does not. Junctional adhesion is the combination of plastic coupling and labile adhesion. (b) sensitivity analysis showing the dependence of the CNV initiation probability upon the strength of the RPE-POS, RPE-BM and RPE-RPE adhesive coupling. Red corresponds to a probability of 1 and purple to a probability of 0. The black region (top-front corner) demarcates the locus of normal adhesion. The isosurfaces correspond to initiation probabilities of 025, 0.5 and 0.75, from front to back. (c) and (d) snapshots from a simulation showing type 1 (sub-RPE) to type 2 (sub-retinal) CNV progression. PIS and POS are light purple, RPE is brown, stalk cells are green, vascular (CC) cells are red and BM is light blue. (c) 3D snapshot at month 6. The open arrow indicates a location at which stalk cells have migrated into the sub-retinal space. (d) 2D snapshot at month 12. The black arrow marks the sub-RPE capillary network, whilst the open arrows mark the sub-retinal capillary network. PIS: photoreceptor inner segment, POS: photoreceptor outer segment, RPE: retinal pigment epithelium, BM: Bruch's membrane, RBaL: basal lamina of the RPE, RBaM: basement membrane of the RPE, CC: choriocapillaris. Figures reproduced, with permission (and modifications in (a) and (b)), from Shirinifard et al. (2012).

in BM are insufficient to initiate CNV when all the adhesions are normal. In addition, neither the threshold for RPE hypoxia, nor RPE hypoxic signalling, affects the results. Thus, the model provides important insights into CNV.

Simulations show good agreement with experimental and clinical data, though there are some discrepancies. For example, the type 1 to type 2 progression has not been observed clinically. It may be that this progression does occur, but that it is difficult to detect, requiring more frequent observations over a longer period of time (Shirinifard et al., 2012).

Future modelling work could include blood flow and its effect on capillary development in a similar way to McDougall et al. (2012) and Watson et al. (2012) (Section 4.1) and perhaps also blood flow within the CC as in Zouache et al. (2015) (Section 3.3, noting that Shirinifard et al.'s model assumes that oxygen levels are constant throughout the blood vessels). Additionally, basal deposits such as hard and soft drusen, together with fibrosis (the formation of extracellular matrix) could also be included in future models (Shirinifard et al., 2012).

Experimental quantification of the adhesivities between the cells of the retina and how these change under pathological conditions would allow more effective validation of the model, together with more clinically accurate predictions. Shirinifard et al. suggest that these measurements could be made non-

invasively by examining changes in RPE and CC morphology, or changes in autofluorescence due to lipid accumulation.

In time, and following extensive trials, this model, or a refined version thereof, could become a useful clinical tool, allowing for more accurate determination of each patient's pathology and, hence, inform the selection of the most appropriate treatment strategy (i.e. personalised medicine). Further, Shirinifard et al. suggest that the model could be continuously improved using data from each clinical or experimental case to which it is applied (e.g. using machine learning).

6. Perspective and Future Directions

The *mathematical* and *computational models* discussed in this paper have uncovered a wealth of insights into retinal physiology and biochemistry, across a range of scenarios, spanning the healthy, developmental and diseased states. Whilst models are developed with a particular state in mind, it is often the case that they may be adapted to examine one or both of the other two states. In particular, many of the models of the healthy and developing retina can be used to explore pathological scenarios.

In the *healthy state*, theoretical models have enabled us to explain the retinal oxygen distribution in terms of the variation in oxygen demand between different retinal layers, allowing the identification of the chief oxygen consumers and an investigation of how consumption varies between light adaptation and dark adaptation. Further, it has been demonstrated that the protein neuroglobin may play an important role in the prevention of hypoxia within the retina, through its ability to transport oxygen from regions where it is rich to those where it is poor, its oxygen affinity being near-optimal for this process. Modelling of blood flow within the choriocapillaris has demonstrated the effect of lobule geometry upon the flow properties within each lobule, suggesting how blood flow will vary across the eye with geographical variation in lobule geometry. This may also be a factor in the spatially heterogeneous progression of diseases such as retinitis pigmentosa (RP) and age-related macular degeneration (AMD). Lastly, it has been demonstrated that the diurnal variation in photoreceptor outer segment (OS) length may be regulated by the oxygen and phosphocreatine shuttle-derived ATP landscape within the photoreceptor, but that neither of these factors in isolation is sufficient to explain this variation. It is shown that inefficiencies in mitochondrial function or OS energy utilisation give rise to OS shortening, a phenomenon observed in many retinal diseases such as RP and AMD.

In the *developing state*, mathematical and computational models of retinal angiogenesis have captured the *in vivo* dynamics of retinal vascular plexus formation with a remarkable degree of accuracy. The importance of perfusion, plexus remodelling, and convected and conducted stimuli for the development of highly structured vascular trees is demonstrated. The model is also used to predict the effect of various parameter values and model components upon development. For example, if the input arterial haematocrit is increased, or the rate of tissue oxygen consumption is decreased, hyperoxia develops, leading to the formation of large capillary-free zones. The former case is equivalent to retinopathy of prematurity and the latter to oxygen induced retinopathy, producing similar predicted outcomes to those seen in these conditions.

In the *diseased state*, mathematical and computational models have been used to investigate RP and choroidal neovascularisation (CNV). In RP, models have explored the trophic factor, toxic substance and oxygen toxicity hypotheses. Trophic factor models demonstrate the rhythmic shedding and renewal of photoreceptors seen *in vivo*. The ratios of cone, normal rod and mutant rod shedding to renewal rates, and trophic factor carrying capacity are found to be key in determining the advancement of RP through various disease states, providing potential clues to treatment. The toxic substance model is able to replicate the exponential decline in photoreceptor number seen in experiments, together with the patchy photoreceptor loss seen in the early stages of RP. The oxygen toxicity model suggests that this mechanism is sufficient to explain some, but not all of the *in vivo* spatio-temporal patterns of degeneration, demonstrating the strengths and weaknesses of this hypothesis. Lastly, the CNV model demonstrates that adhesion failures between outer retinal components, together with the presence of a tip cell, are necessary and sufficient conditions for CNV to initiate.

The above studies demonstrate the power of mathematical and computational modelling in investigating the structure and function of the retina. Despite the advances which have been made, theoretical modelling has yet to achieve its full potential in this area, current work representing merely the tip of the iceberg, given the possibilities which have yet to be explored. In the healthy state, much work remains to be done in modelling processes such as the visual cycle, photoreceptor-RPE interactions, pre-processing of visual information by the retina and aging of the retina. In development, there is scope for extensive work targeted at understanding how the complex layered structure of the retina arises, including retinal mosaic formation, together with the establishment of the full 3D structure of the retinal capillary layers. Many retinal diseases start to take effect during the developmental stage, therefore extensive modelling of retinal development will be required in order to fully understand these pathologies. Substantial further work remains for RP and AMD, whilst other disease states such as diabetic retinopathy, retinopathy of prematurity and retinoblastoma are largely untouched. Ultimately, the aim would be to produce a collection of validated models, individually detailing an important aspect of the retina, which can subsequently be coupled, as required, to enable retinal modelling that can encompass development, health and the full range of disease states. These could then be used as clinical tools, to inform personalised treatment strategies.

In order to achieve these aims, greater attention to this area is required from the mathematical and computational modelling communities, together with an increase in ophthalmic clinicians and experimentalists ready to work with theoreticians to parametrise and validate their models and to test model predictions (thus completing the experiment/modelling cycle, see Figure 1). At present, whilst a lot of data are available on the retina, many of the parameters which are key to forming accurate models have yet to be precisely measured, despite advances in ex-

perimental, diagnostic and imaging techniques rendering these measurements tractable. As experimental/theoretical collaborations increase, so too will the insights which can be obtained into the retina, making possible discoveries which neither set of disciplines could have achieved on its own.

Acknowledgements

We gratefully acknowledge the Engineering and Physical Sciences Research Council (EPSRC) in the UK for funding through a studentship at the Systems Biology programme of the University of Oxford's Doctoral Training Centre P.A.R. We also thank the anonymous reviewers for their helpful and insightful comments.

References

Abrámoff, M. D., Mullins, R. F., Lee, K., Hoffmann, J. M., Sonka, M., Critser, D. B., Stasheff, S. F., Stone, E. M., 2013. Human photoreceptor outer segments shorten during light adaptation. Invest. Ophthalmol. Vis. Sci. 54 (5), 3721–3728.

Al-Diri, B., Hunter, A., Steel, D., Habib, M., 2010. Automated analysis of retinal vascular network connectivity. Comput. Med. Imag. Grap. 34 (6), 462–470.

Aletti, M., Gerbeau, J. F., Lombardi, D., 2015. Modeling autoregulation in three-dimensional simulations of retinal hemodynamics. J. Model. Ophthalmol. 1.

Ames, B. N., Shigenaga, M. K., Hagen, T. M., 1993. Oxidants, antioxidants, and the degenerative diseases of aging. Proc. Natl. Acad. Sci. 90 (17), 7915–7922.

Ames, B. N., Shigenaga, M. K., Hagen, T. M., 1995. Mitochondrial decay in aging. Biochim. Biophys. Acta. 1271 (1), 165–170.

Anderson, B., 1968. Ocular effects of changes in oxygen and carbon dioxide tension. Trans. Am. Ophthalmol. Soc. 66, 423–474.

Anderson, B., Saltzman, H. A., 1964. Retinal oxygen utilization measured by hyperbaric blackout. Arch. Ophthalmol. 72 (6), 792–795.

Arciero, J., Harris, A., Siesky, B., Amireskandari, A., Gershuny, V., Pickrell, A., Guidoboni, G., 2013. Theoretical analysis of vascular regulatory mechanisms contributing to retinal blood flow autoregulation. Invest. Ophthalmol. Vis. Sci. 54 (8), 5584–5593.

Aubert, M., Chaplain, M. A. J., McDougall, S. R., Devlin, A., Mitchell, C. A., 2011. A continuum mathematical model of the developing murine retinal vasculature. Bull. Math. Biol. 73, 2430–2451.

Band, L. R., Hall, C. L., Richardson, G., Jensen, O. E., Siggers, J. H., Foss, A. J. E., 2009. Intracellular flow in optic nerve axons: A mechanism for cell death in glaucoma. Invest. Ophthalmol. Vis. Sci. 50 (8), 3750–3758.

Barton, A., Fendrik, A. J., 2015. Retinogenesis: Stochasticity and the competency model. J. Theor. Biol. 373 (0), 73–81.

Bassi, C. J., Powers, M. K., 1990. Shedding of rod outer segments is light-driven in goldfish. Invest. Ophthalmol. Vis. Sci. 31 (11), 2314–2319.

Braun, R. D., Linsenmeier, R. A., Goldstick, T. K., 1995. Oxygen consumption in the inner and outer retina of the cat. Invest. Ophthalmol. Vis. Sci. 36 (3), 542–554.

Braun, R. J., 2012. Dynamics of the tear film. Annu. Rev. Fluid Mech. 44 (1), 267–297.

Braun, R. J., King-Smith, P. E., Begley, C. G., Li, L., Gewecke, N. R., 2015. Dynamics and function of the tear film in relation to the blink cycle. Prog. Retin. Eye. Res. 45, 132–164.

Brunori, M., Vallone, B., 2007. Neuroglobin, seven years after. Cell. Mol. Life Sci. 64, 1259–1268.

Burd, H. J., Regueiro, R. A., 2015. Finite element implementation of a multiscale model of the human lens capsule. Biomech. Model Mechanobiol., 1–16.

Burgoyne, C. F., Crawford Downs, J., Bellezza, A. J., Francis Suh, J. K., Hart, R. T., 2005. The optic nerve head as a biomechanical structure: a new paradigm for understanding the role of IOP-related stress and strain in the pathophysiology of glaucomatous optic nerve head damage. Prog. Retin. Eye Res. 24 (1), 39–73.

Burmester, T., Hankeln, T., 2004. Neuroglobin: A respiratory protein of the nervous system. News Physiol. Sci. 19 (3), 110–113.

Burmester, T., Hankeln, T., 2009. What is the function of neuroglobin? J. Exp. Biol. 212 (10), 1423–1428.

Burmester, T., Weich, B., Reinhardt, S., Hankeln, T., 2000. A vertebrate globin expressed in the brain. Nature 407 (6803), 520–523.

Burns, J., Clarke, G., Lumsden, C. J., 2002. Photoreceptor death: Spatiotemporal patterns arising from one-hit death kinetics and a diffusible cell death factor. Bull. Math. Biol. 64, 1117–1145.

Camacho, E., Rand, R., Howland, H., 2004. Dynamics of two van der Pol oscillators coupled via a bath. Int. J. Solids Struct. 41 (8), 2133–2143.

Camacho, E. T., Colón Vélez, M. A., Hernández, D. J., Bernier, U. R., van Laarhoven, J., Wirkus, S., 2010. A mathematical model for photoreceptor interactions. J. Theor. Biol. 267 (4), 638–646.

Camacho, E. T., Melara, L. A., Villalobos, M. C., Wirkus, S., 2014. Optimal control in the treatment of retinitis pigmentosa. Bull. Math. Biol. 76 (2), 292–313.

Camacho, E. T., Wirkus, S., 2013. Tracing the progression of retinitis pigmentosa via photoreceptor interactions. J. Theor. Biol. 317 (0), 105–118.

Causin, P., Guidoboni, G., Malgaroli, F., Sacco, R., Harris, A., 2015. Blood flow mechanics and oxygen transport and delivery in the retinal microcirculation: multiscale mathematical modeling and numerical simulation. Biomech. Model Mechanobiol.

Chan, G., Balaratnasingam, C., Yu, P. K., Morgan, W. H., McAllister, I. L., Cringle, S. J., Yu, D.-Y., 2012. Quantitative morphometry of perifoveal capillary networks in the human retina. Invest. Ophthalmol. Vis. Sci. 53 (9), 5502–5514.

Cideciyan, A. V., Hood, D. C., Huang, Y., Banin, E., Li, Z.-Y., Stone, E. M., Milam, A. H., Jacobson, S. G., 1998. Disease sequence from mutant rhodopsin allele to rod and cone photoreceptor degeneration in man. Proc. Natl. Acad. Sci. 95 (12), 7103–7108.

Clarke, G., Collins, R. A., Leavitt, B. R., Andrews, D. F., Hayden, M. R., Lumsden, C. J., McInnes, R. R., 2000. A one-hit model of cell death in inherited neuronal degenerations. Nature 406, 195–199.

Clarke, G., Lumsden, C. J., 2005a. Heterogeneous cellular environments modulate one-hit neuronal death kinetics. Brain Res. Bull. 65 (1), 59–67.

Clarke, G., Lumsden, C. J., 2005b. Scale-free neurodegeneration: cellular heterogeneity and the stretched exponential kinetics of cell death. J. Theor. Biol. 233 (4), 515–525.

Clarke, G., Lumsden, C. J., McInnes, R. R., 2001. Inherited neurodegenerative diseases: the one-hit model of neurodegeneration. Hum. Mol. Genet. 10 (20), 2269–2275.

Coleman, H. R., Chan, C. C., Ferris III, F. L., Chew, E. Y., 2008. Age-related macular degeneration. Lancet 372 (9652), 1835–1845.

Colón Vélez, M. A., Hernández, D. J., Bernier, U. R., van Laarhoven, J., Camacho, E. T., 2003. Mathematical models for photoreceptor interactions. Tech. rep., Cornell University, Department of Biological Statistics and Computational Biology.

Connor, A. J., Nowak, R. P., Lorenzon, E., Thomas, M., Herting, F., Hoert, S., Quaiser, T., Shochat, E., Pitt-Francis, J., Cooper, J., Maini, P. K., Byrne, H. M., 2015. An integrated approach to quantitative modelling in angiogenesis research. J. R. Soc. Interface 12 (110).

Cringle, S., Yu, D. Y., Alder, V., Su, E. N., Yu, P., 1996. Oxygen consumption in the avascular guinea pig retina. Am. J. Physiol. Heart. Circ. Physiol. 271 (3), H1162–H1165.

Cringle, S. J., Yu, D. Y., 2002. A multi-layer model of retinal oxygen supply and consumption helps explain the muted rise in inner retinal PO(2) during systemic hyperoxia. Comp. Biochem. Physiol. 132 (1), 61–66.

David, T., Moore, S., 2008. Modeling perfusion in the cerebral vasculature. Med. Eng. Phys. 30 (10), 1227–1245.

de Vries, G., Hillen, T., Lewis, M. A., Müller, J., Schönfisch, B., 2006. A Course in Mathematical Biology: Quantitative Modeling with Mathematical and Computational Methods. Monographs on Mathematical Modeling and Computation. SIAM publishing.

Dollery, C. T., Bulpitt, C. J., Kohner, E. M., 1969. Oxygen supply to the retina from the retinal and choroidal circulations at normal and increased arterial oxygen tensions. Invest. Ophthalmol. Vis. Sci. 8 (6), 588–594.

Eglen, S. J., 2006. Development of regular cellular spacing in the retina: theoretical models. Math. Med. Biol. 23 (2), 79–99.

Eglen, S. J., 2012. Cellular spacing: Analysis and modelling of retinal mosaics. In: Le Novère, N. (Ed.), Computational Systems Neurobiology. Springer, Ch. 12, pp. 365–385.

Ethier, C. R., Johnson, M., Ruberti, J., 2004. Ocular biomechanics and biotransport. Annu. Rev. Biomed. Eng. 6 (1), 249–273.

Fago, A., Hundahl, C., Malte, H., Weber, R. E., 2004. Functional properties of neuroglobin and cytoglobin. insights into the ancestral physiological roles of globins. IUBMB Life 56 (11-12), 689–696.

Filas, B. A., Shui, Y. B., Beebe, D. C., 2013. Computational model for oxygen transport and consumption in human vitreous. Invest. Ophthalmol. Vis. Sci. 54 (10), 6549–6559.

Fintz, A. C., Audo, I., Hicks, D., Mohand-Saïd, S., Léveillard, T., Sahel, J., 2003. Partial characterization of retina-derived cone neuroprotection in two culture models of photoreceptor degeneration. Invest. Ophthalmol. Vis. Sci. 44 (2), 818–825.

Flower, R. W., von Kerczek, C., Zhu, L., Ernest, A., Eggleton, C., Topoleski, L. D. T., 2001. Theoretical investigation of the role of choriocapillaris blood flow in treatment of subfoveal choroidal neovascularization associated with age-related macular degeneration. Am. J. Ophthalmol. 132 (1), 85–93.

Friedland, A. B., 1978. A mathematical model of transmural transport of oxygen to the retina. Bull. Math. Biol. 40 (6), 823–837.

Friedman, E., Smith, T. R., Kuwabara, T., 1963. Senile choroidal vascular patterns and drusen. Arch. Ophthalmol. 69 (2), 220–230.

Ganesan, P., He, S., Xu, H., 2010a. Analysis of retinal circulation using an image-based network model of retinal vasculature. Microvasc. Res. 80 (1), 99–109.

Ganesan, P., He, S., Xu, H., 2010b. Development of an image-based network model of retinal vasculature. Ann. Biomed. Eng. 38, 1566–1585.

García-Ayuso, D., Ortín-Martínez, A., Jiménez-López, M., Galindo-Romero, C., Cuenca, N., Pinilla, I., Vidal-Sanz, M., Agudo-Barriuso, M., Villegas-Pérez, M. P., 2013. Changes in the photoreceptor mosaic of P23H-1 rats during retinal degeneration: Implications for rod-cone dependent survival. Invest. Ophthalmol. Vis. Sci. 54 (8), 5888–5900.

Giachetti, A., Ballerini, L., Trucco, E., 2014. Accurate and reliable segmentation of the optic disc in digital fundus images. J. Med. Imag. 1 (2).

Grover, S., Fishman, G. A., Brown Jr, J., 1998. Patterns of visual field progression in patients with retinitis pigmentosa. Ophthalmology 105 (6), 1069–1075.

Grytz, R., Meschke, G., 2010. A computational remodeling approach to predict the physiological architecture of the collagen fibril network in corneo-scleral shells. Biomech. Model Mechanobiol. 9 (2), 225–235.

Grytz, R., Meschke, G., Jonas, J. B., 2011. The collagen fibril architecture in the lamina cribrosa and peripapillary sclera predicted by a computational remodeling approach. Biomech. Model Mechanobiol. 10 (3), 371–382.

Guidoboni, G., Harris, A., Cassani, S., Arciero, J., Siesky, B., Amireskandari, A., Tobe, L., Egan, P., Januleviciene, I., Park, J., 2014. Intraocular pressure, blood pressure, and retinal blood flow autoregulation: A mathematical model to clarify their relationship and clinical relevance. Invest. Ophthalmol. Vis. Sci. 55 (7), 4105–4118.

Hamel, C., 2006. Retinitis pigmentosa. Orphanet. J. Rare Dis. 1 (1), 40.

Hamel, C., 2007. Cone rod dystrophies. Orphanet. J. Rare Dis. 2 (1), 7.

Harris, A., Guidoboni, G., Arciero, J. C., Amireskandari, A., Tobe, L. A., Siesky, B. A., 2013. Ocular hemodynamics and glaucoma: The role of mathematical modeling. Eur. J. Ophthalmol. 23 (2), 139–146.

Hartong, D. T., Berson, E. L., Dryja, T. P., 2006. Retinitis pigmentosa. Lancet 368 (9549), 1795–1809.

Hassenstein, A., Meyer, C. H., 2009. Clinical use and research applications of Heidelberg retinal angiography and spectral-domain optical coherence tomography - a review. Clin. Experiment. Ophthalmol. 37 (1), 130–143.

Haugh, L., Linsenmeier, R., Goldstick, T., 1990. Mathematical models of the spatial distribution of retinal oxygen tension and consumption, including changes upon illumination. Ann. Biomed. Eng. 18, 19–36.

Howison, S., 2005. Practical Applied Mathematics: Modelling, Analysis, Approximation. Cambridge Texts in Applied Mathematics. Cambridge University Press.

Hsu, R., Secomb, T. W., 1989. A Green's function method for analysis of oxygen delivery to tissue by microvascular networks. Math. Biosci. 96 (1), 61–78.

Jackson, T., Zheng, X., 2010. A cell-based model of endothelial cell migration, proliferation and maturation during corneal angiogenesis. Bull. Math. Biol. 72, 830–868.

Jager, R. D., Mieler, W. F., Miller, J. W., 2008. Age-related macular degeneration. N. Engl. J. Med. 358 (24), 2606–2617.

Ji, Y., Zhu, C. L., Grzywacz, N. M., Lee, E. J., 2012. Rearrangement of the cone mosaic in the retina of the rat model of retinitis pigmentosa. J. Comp. Neurol. 520 (4), 874–888.

Jiann, L. Y., Ismail, Z., Shafie, S., Fitt, A., 2015. Numerical computational of fluid flow through a detached retina. AIP Conference Proceedings 1643 (1), 642–648.

Jiao, Y., Lau, T., Hatzikirou, H., Meyer-Hermann, M., Corbo, J. C., Torquato, S., 2014. Avian photoreceptor patterns represent a disordered hyperuniform solution to a multiscale packing problem. Phys. Rev. E 89, 022721.

Keane, P. A., Sadda, S. R., 2014. Retinal imaging in the twenty-first century: State of the art and future directions. Ophthalmology 121 (12), 2489–2500.

Keener, J., Sneyd, J., 2009a. Mathematical Physiology I: Cellular Physiology, 2nd Edition. Interdisciplinary Applied Mathematics. Springer.

Keener, J., Sneyd, J., 2009b. Mathematical Physiology II: Systems Physiology, 2nd Edition. Interdisciplinary Applied Mathematics. Springer.

King-Smith, P. E., Nichols, J. J., Nichols, K. K., Fink, B. A., Braun, R. J., 2008. Contributions of evaporation and other mechanisms to tear film thinning and break-up. Optometry & Vision Science 85 (8), 623–630.

Kohen, R., Nyska, A., 2002. Invited review: Oxidation of biological systems: Oxidative stress phenomena, antioxidants, redox reactions, and methods for their quantification. Toxicol. Pathol. 30 (6), 620–650.

Kranz, K., Paquet-Durand, F., Weiler, R., Janssen-Bienhold, U., Dedek, K., 2013. Testing for a gap junction-mediated bystander effect in retinitis pigmentosa: Secondary cone death is not altered by deletion of connexin36 from cones. PLoS One 8 (2), e57163.

Krogh, A., 1919. The number and distribution of capillaries in muscles with calculations of the oxygen pressure head necessary for supplying the tissue. J. Physiol. 52 (6), 409–415.

Kur, J., Newman, E. A., Chan-Ling, T., 2012. Cellular and physiological mechanisms underlying blood flow regulation in the retina and choroid in health and disease. Prog. Retin. Eye. Res. 31 (5), 377–406.

Lamb, T. D., Pugh Jr., E. N., 2004. Dark adaptation and the retinoid cycle of vision. Prog. Retin. Eye. Res. 23 (3), 307–380.

Lee, E. J., Ji, Y., Zhu, C. L., Grzywacz, N. M., 2011. Role of Müller cells in cone mosaic rearrangement in a rat model of retinitis pigmentosa. Glia 59 (7), 1107–1117.

Leontidis, G., Al-Diri, B., Hunter, A., 2014. Diabetic retinopathy: current and future methods for early screening from a retinal hemodynamic and geometric approach. Expert Rev. Ophthalmol. 9 (5), 431–442.

Léveillard, T., Mohand-Saïd, S., Lorentz, O., Hicks, D., Fintz, A. C., Clérin, E., Simonutti, M., Forster, V., Cavusoglu, N., Chalmel, F., Dollé, P., Poch, O., Lambrou, G., Sahel, J. A., 2004. Identification and characterization of rod-derived cone viability factor. Nat. Genet. 36 (7), 755–759.

Linsenmeier, R. A., 1986. Effects of light and darkness on oxygen distribution and consumption in the cat retina. J. Gen. Physiol. 88 (4), 521–542.

Liu, B. S., Tarima, S., Visotcky, A., Pechauer, A., Cooper, R. F., Landsem, L., Wilk, M. A., Godara, P., Makhijani, V., Sulai, Y. N., Syed, N., Yasumura, G., Garg, A. K., Pennesi, M. E., Lujan, B. J., Dubra, A., Duncan, J. L., Carroll, J., 2014. The reliability of parafoveal cone density measurements. Br. J. Ophthalmol. 98 (8), 1126–1131.

Liu, D., Wood, N. B., Witt, N., Hughes, A. D., Thom, S. A., Xu, X. Y., 2009. Computational analysis of oxygen transport in the retinal arterial network. Curr. Eye Res. 34 (11), 945–956.

Lomasko, T., Clarke, G., Lumsden, C. J., 2007a. One-hit stochastic decline in a mechanochemical model of cytoskeleton-induced neuron death I: Cell-fate arrival times. J. Theor. Biol. 249 (1), 1–17.

Lomasko, T., Clarke, G., Lumsden, C. J., 2007b. One-hit stochastic decline in a mechanochemical model of cytoskeleton-induced neuron death II: Transition state metastability. J. Theor. Biol. 249 (1), 18–28.

Lomasko, T., Lumsden, C. J., 2009. One-hit stochastic decline in a mechanochemical model of cytoskeleton-induced neuron death III: Diffusion pulse death zones. J. Theor. Biol. 256 (1), 104–116.

Macdougall, L., 2015. Mathematical modelling of retinal metabolism. Ph.D. thesis, University of Nottingham.

Maggelakis, S. A., Savakis, A. E., 1996. A mathematical model of growth factor induced capillary growth in the retina. Mathl. Comput. Modelling 24 (7), 33–41.

Maggelakis, S. A., Savakis, A. E., 1999. A mathematical model of retinal neovascularization. Mathl. Comput. Modelling 29 (2), 91–97.

McDougall, S. R., Watson, M. G., Devlin, A. H., Mitchell, C. A., Chaplain, M. A. J., 2012. A hybrid discrete-continuum mathematical model of pattern prediction in the developing retinal vasculature. Bull. Math. Biol. 74, 2272–2314.

McGuire, B. J., Secomb, T. W., 2001. A theoretical model for oxygen transport in skeletal muscle under conditions of high oxygen demand. J. Appl. Physiol. 91 (5), 2255–2265.

Mervin, K., Stone, J., 2002. Regulation by oxygen of photoreceptor death in the developing and adult C57BL/6J mouse. Exp. Eye Res. 75 (6), 715–722.

Meskauskas, J., Repetto, R., Siggers, J. H., 2012. Shape change of the vitreous chamber influences retinal detachment and reattachment processes: Is mechanical stress during eye rotations a factor? Invest. Ophthalmol. Vis. Sci. 53 (10), 6271–6281.

Michaelson, I., 1954. Retinal circulation in man and animals. Thomas.

Mohand-Saïd, S., Deudon-Combe, A., Hicks, D., Simonutti, M., Forster, V., Fintz, A. C., Léveillard, T., Dreyfus, H., Sahel, J. A., 1998. Normal retina releases a diffusible factor stimulating cone survival in the retinal degeneration mouse. Proc. Natl. Acad. Sci. 95 (14), 8357–8362.

Mohand-Saïd, S., Hicks, D., Dreyfus, H., Sahel, J. A., 2000. Selective transplantation of rods delays cone loss in a retinitis pigmentosa model. Arch. Ophthalmol. 118 (6), 807–811.

Mohand-Saïd, S., Hicks, D., Simonutti, M., Tran-Minh, D., Deudon-Combe, A., Dreyfus, H., Silverman, M. S., Ogilvie, J. M., Tenkova, T., Sahel, J., 1997. Photoreceptor transplants increase host cone survival in the retinal degeneration (rd) mouse. Ophthalmic Res. 29, 290–297.

Morton, K. W., Mayers, D. F., 2005. Numerical Solution of Partial Differential Equations: An Introduction. Cambridge University Press.

Murakami, T., Akimoto, M., Ooto, S., Suzuki, T., Ikeda, H., Kawagoe, N., Takahashi, M., Yoshimura, N., 2008. Association between abnormal autofluorescence and photoreceptor disorganization in retinitis pigmentosa. Am. J. Ophthalmol. 145 (4), 687–694.

Murray, J. D., 2002. Mathematical Biology I: An Introduction, 3rd Edition. Interdisciplinary Applied Mathematics. Springer.

Murray, J. D., 2003. Mathematical Biology II: Spatial Models and Biomedical Applications, 3rd Edition. Interdisciplinary Applied Mathematics. Springer.

Pellegrini, E., Robertson, G., Trucco, E., MacGillivray, T. J., Lupascu, C., van Hemert, J., Williams, M. C., Newby, D. E., van Beek, E. J., Houston, G., 2014. Blood vessel segmentation and width estimation in ultra-wide field scanning laser ophthalmoscopy. Biomed. Opt. Express 5 (12), 4329–4337.

Pesce, A., Bolognesi, M., Bocedi, A., Ascenzi, P., Dewilde, S., Moens, L., Hankeln, T., Burmester, T., 2002. Neuroglobin and cytoglobin. fresh blood for the vertebrate globin family. EMBO Rep. 3 (12), 1146–1151.

Pournaras, C. J., Rungger-Brändle, E., Riva, C. E., Hardarson, S. H., Stefansson, E., 2008. Regulation of retinal blood flow in health and disease. Prog. Retin. Eye. Res. 27 (3), 284–330.

Ripps, H., 2002. Cell death in retinitis pigmentosa: Gap junctions and the 'bystander' effect. Exp. Eye Res. 74 (3), 327–336.

Roberts, P. A., 2015. Mathematical models of the retina in health and disease. D.Phil. thesis, University of Oxford.

Roberts, P. A., Gaffney, E. A., Luthert, P. J., Foss, A. J. E., Byrne, H. M., 2015. Retinal oxygen distribution and the role of neuroglobin. J. Math. Biol.

Robson, A. G., Saihan, Z., Jenkins, S. A., Fitzke, F. W., Bird, A. C., Webster, A. R., Holder, G. E., 2006. Functional characterisation and serial imaging of abnormal fundus autofluorescence in patients with retinitis pigmentosa and normal visual acuity. Br. J. Ophthalmol. 90 (4), 472–479.

Rossi, T., Boccassini, B., Esposito, L., Clemente, C., Iossa, M., Placentino, L., Bonora, N., 2012. Primary blast injury to the eye and orbit: Finite element modeling. Invest. Ophthalmol. Vis. Sci. 53 (13), 8057–8066.

Ruberti, J. W., Roy, A. S., Roberts, C. J., 2011. Corneal biomechanics and biomaterials. Annu. Rev. Biomed. Eng. 13 (1), 269–295.

Safaeian, N., David, T., 2013. A computational model of oxygen transport in the cerebrocapillary levels for normal and pathologic brain function. J. Cereb. Blood Flow Metab. 33 (10), 1633–1641.

Salbreux, G., Barthel, L. K., Raymond, P. A., Lubensky, D. K., 2012. Coupling mechanical deformations and planar cell polarity to create regular patterns in the zebrafish retina. PLoS Comput. Biol. 8 (8), e1002618.

Secomb, T. W., 2015. A Green's function method for simulation of time-dependent solute transport and reaction in realistic microvascular geometries. Math. Med. Biol.

Secomb, T. W., Hsu, R., Dewhirst, M. W., Klitzman, B., Gross, J. F., 1993. Analysis of oxygen transport to tumor tissue by microvascular networks. Int. J. Radiation Oncology Biol. Phys. 25 (3), 481–489.

Secomb, T. W., Hsu, R., Park, E. Y. H., Dewhirst, M. W., 2004. Green's function methods for analysis of oxygen delivery to tissue by microvascular networks. Ann. Biomed. Eng. 32 (11), 1519–1529.

Seth, D., 2012. An analytical solution for diffusion and nonlinear uptake of oxygen in the retina. IJM2C 2 (3), 181–188.

Shen, J., Yang, X., Dong, A., Petters, R. M., Peng, Y. W., Wong, F., Campochiaro, P. A., 2005. Oxidative damage is a potential cause of cone cell death in retinitis pigmentosa. J. Cell Physiol. 203 (3), 457–464.

Shintani, K., Shechtman, D. L., Gurwood, A. S., 2009. Review and update: Current treatment trends for patients with retinitis pigmentosa. Optometry 80 (7), 384–401.

Shirinifard, A., Glazier, J. A., Swat, M., Gens, J. S., Family, F., Jiang, Y., Grossniklaus, H. E., 2012. Adhesion failures determine the pattern of choroidal neovascularization in the eye: A computer simulation study. PLoS Comput. Biol. 8 (5), e1002440.

Sigal, I. A., Ross Ethier, C., 2009. Biomechanics of the optic nerve head. Exp. Eye Res. 88 (4), 799–807.

Siggers, J. H., Ethier, C. R., 2012. Fluid mechanics of the eye. Annu. Rev. Fluid Mech. 44 (1), 347–372.

Sneyd, J., Tranchina, D., 1989. Phototransduction in cones: An inverse problem in enzyme kinetics. Bull. Math. Biol. 51 (6), 749–784.

Snodderly, D. M., Weinhaus, R. S., Choi, J. C., 1992. Neural-vascular relationships in central retina of macaque monkeys (Macaca fascicularis). J. Neurosci. 12 (4), 1169–1193.

Song, Z., Coca, D., Billings, S., Postma, M., Hardie, R. C., Juusola, M., 2009. Biophysical modeling of a drosophila photoreceptor. In: Leung, C. S., Lee, M., Chan, J. H. (Eds.), Neural Information Processing. Vol. 5863 of Lecture Notes in Computer Science. Springer Berlin Heidelberg, pp. 57–71.

Song, Z., Postma, M., Billings, S., Coca, D., Hardie, R., Juusola, M., 2012. Stochastic, adaptive sampling of information by microvilli in fly photoreceptors. Curr. Biol. 22 (15), 1371–1380.

Stefánsson, E., 1988. Retinal oxygen tension is higher in light than dark. Pediatr. Res. 23, 5–8.

Stewart, P. S., Jensen, O. E., Foss, A. J. E., 2014. A theoretical model to allow prediction of the CSF pressure from observations of the retinal venous pulse. Invest. Ophthalmol. Vis. Sci. 55 (10), 6319–6323.

Stone, J., Maslim, J., Valter-Kocsi, K., Mervin, K., Bowers, F., Chu, Y., Barnett, N., Provis, J., Lewis, G., Fisher, S. K., Bistid, S., Gargini, C., Cervetto, L., Merin, S., Pe'er, J., 1999. Mechanisms of photoreceptor death and survival in mammalian retina. Prog. Retin. Eye Res. 18(6), 689–735.

Strogatz, S. H., 1994. Nonlinear Dynamics and Chaos: With Applications to Physics, Biology, Chemistry, and Engineering. Advanced book program. Westview Press.

Süli, E., Mayers, D. F., 2003. An Introduction to Numerical Analysis. Cambridge University Press.

Swaroop, A., Kim, D., Forrest, D., 2010. Transcriptional regulation of photoreceptor development and homeostasis in the mammalian retina. Nat. Rev. Neurosci. 11, 563–576.

Tan, P. E. Z., Yu, P. K., Balaratnasingam, C., Cringle, S. J., Morgan, W. H., McAllister, I. L., Yu, D.-Y., 2012. Quantitative confocal imaging of the retinal microvasculature in the human retina. Invest. Ophthalmol. Vis. Sci. 53 (9), 5728–5736.

Till, S. J., Till, J., Milsom, P. K., Rowlands, G., 2003. A new model for laser-induced thermal damage in the retina. Bull. Math. Biol. 65 (4), 731–746.

Tranchina, D., Sneyd, J., Cadenas, I. D., 1991. Light adaptation in turtle cones. testing and analysis of a model for phototransduction. Biophys. J. 60 (1), 217–237.

Travis, G. H., Sutcliffe, J. G., Bok, D., 1991. The retinal degeneration slow (rds) gene product is a photoreceptor disc membrane-associated glycoprotein. Neuron 6 (1), 61–70.

Valter, K., Maslim, J., Bowers, F., Stone, J., 1998. Photoreceptor dystrophy in the RCS rat: roles of oxygen, debris, and bFGF. Invest. Ophthalmol. Vis. Sci. 39 (12), 2427–2442.

van Velthoven, M. E. J., Faber, D. J., Verbraak, F. D., van Leeuwen, T. G., de Smet, M. D., 2007. Recent developments in optical coherence tomography for imaging the retina. Prog. Retin. Eye. Res. 26 (1), 57–77.

Wangsa-Wirawan, N. D., Linsenmeier, R. A., 2003. Retinal oxygen: Fundamental and clinical aspects. Arch. Ophthalmol. 121 (4), 547–557.

Watson, M. G., McDougall, S. R., Chaplain, M. A. J., Devlin, A. H., Mitchell, C. A., 2012. Dynamics of angiogenesis during murine retinal development:

a coupled in vivo and in silico study. J. R. Soc. Interface 9 (74), 2351–2364.
Yang, Y., Mohand-Said, S., Danan, A., Simonutti, M., Fontaine, V., Clerin, E., Picaud, S., Leveillard, T., Sahel, J. A., 2009. Functional cone rescue by RdCVF protein in a dominant model of retinitis pigmentosa. Mol. Ther. 17 (5), 787–795.
Yannuzzi, L. A., Ober, M. D., Slakter, J. S., Spaide, R. F., Fisher, Y. L., Flower, R. W., Rosen, R., 2004. Ophthalmic fundus imaging: today and beyond. Am. J. Ophthalmol. 137 (3), 511–524.
Young, R. W., 1967. The renewal of photoreceptor cell outer segments. J. Cell Biol. 33 (1), 61–72.
Young, R. W., 1971. The renewal of rod and cone outer segments in the rhesus monkey. J. Cell Biol. 49, 303–318.
Young, R. W., 1978. The daily rhythm of shedding and degradation of rod and cone outer segment membranes in the chick retina. Invest. Ophthalmol. Vis. Sci. 17 (2), 105–16.
Young, R. W., Bok, D., 1969. Participation of the retinal pigment epithelium in the rod outer segment renewal process. J. Cell Biol. 42, 392–403.
Yu, D. Y., Cringle, S., Valter, K., Walsh, N., Lee, D., Stone, J., 2004. Photoreceptor death, trophic factor expression, retinal oxygen status, and photoreceptor function in the P23H rat. Invest. Ophthalmol. Vis. Sci. 45 (6), 2013–2019.
Yu, D. Y., Cringle, S. J., 2001. Oxygen distribution and consumption within the retina in vascularised and avascular retinas and in animal models of retinal disease. Prog. Retin. Eye Res. 20 (2), 175–208.
Yu, D. Y., Cringle, S. J., 2002. Outer retinal anoxia during dark adaptation is not a general property of mammalian retinas. Comp. Biochem. Physiol. 132 (1), 47–52.
Yu, D. Y., Cringle, S. J., 2005. Retinal degeneration and local oxygen metabolism. Exp. Eye Res. 80 (6), 745–751.
Yu, D. Y., Cringle, S. J., Balaratnasingam, C., Morgan, W. H., Yu, P. K., Su, E. N., 2013. Retinal ganglion cells: Energetics, compartmentation, axonal transport, cytoskeletons and vulnerability. Prog. Retin. Eye Res. 36, 217–246.
Yu, P. K., Balaratnasingam, C., Morgan, W. H., Cringle, S. J., McAllister, I. L., Yu, D. Y., 2010. The structural relationship between the microvasculature, neurons, and glia in the human retina. Invest. Ophthalmol. Vis. Sci. 51 (1), 447–458.
Zhu, C. L., Ji, Y., Lee, E.-J., Grzywacz, N. M., 2013. Spatiotemporal pattern of rod degeneration in the S334ter-line-3 rat model of retinitis pigmentosa. Cell Tissue Res. 351 (1), 29–40.
Zouache, M., Eames, I., Luthert, P., 7 2015. Blood flow in the choriocapillaris. J. Fluid Mech. 774, 37–66.